BAZ2A safeguards genome architecture of ground-state pluripotent stem cells

Damian Dalcher[1,2], Jennifer Yihong Tan[3] (iD), Cristiana Bersaglieri[1,2], Rodrigo Peña-Hernández[1,2], Eva Vollenweider[1,2], Stefan Zeyen[1,2], Marc W Schmid[4], Valerio Bianchi[5], Stefan Butz[1,2], Marcin Roganowicz[1,2], Rostyslav Kuzyakiv[1,4], Tuncay Baubec[1] (iD), Ana Claudia Marques[3] (iD) & Raffaella Santoro[1,*] (iD)

Abstract

Chromosomes have an intrinsic tendency to segregate into compartments, forming long-distance contacts between loci of similar chromatin states. How genome compartmentalization is regulated remains elusive. Here, comparison of mouse ground-state embryonic stem cells (ESCs) characterized by open and active chromatin, and advanced serum ESCs with a more closed and repressed genome, reveals distinct regulation of their genome organization due to differential dependency on BAZ2A/TIP5, a component of the chromatin remodeling complex NoRC. On ESC chromatin, BAZ2A interacts with SNF2H, DNA topoisomerase 2A (TOP2A) and cohesin. BAZ2A associates with chromatin subdomains within the active A compartment, which intersect through long-range contacts. We found that ground-state chromatin selectively requires BAZ2A to limit the invasion of active domains into repressive compartments. BAZ2A depletion increases chromatin accessibility at B compartments. Furthermore, BAZ2A regulates H3K27me3 genome occupancy in a TOP2A-dependent manner. Finally, ground-state ESCs require BAZ2A for growth, differentiation, and correct expression of developmental genes. Our results uncover the propensity of open chromatin domains to invade repressive domains, which is counteracted by chromatin remodeling to establish genome partitioning and preserve cell identity.

Introduction

The 3D genome organization is functionally important for correct execution of gene expression programs. Chromosomes have an intrinsic tendency to segregate into compartments based on the local epigenetic landscape and transcriptional activity. At the megabase scale, the genome can be divided into two compartments, called A and B compartments, which are estimated by an eigenvector analysis of the genome contact matrix after normalization by the observed-expected method (Lieberman-Aiden *et al*, 2009). Genomic contacts predominately occur between loci belonging to the same compartment. Compartment A is highly enriched for open and active chromatin whereas compartment B is enriched for closed and repressed chromatin. Furthermore, long-distance contacts have been shown to occur between domains with similar chromatin states (Rao *et al*, 2014). Removal or depletion of chromatin-associated cohesin eliminates all loop domains and increased compartmentalization (Haarhuis *et al*, 2017; Nora *et al*, 2017; Rao *et al*, 2017; Schwarzer *et al*, 2017). The opposite effect was achieved by increasing the residence time of cohesins on DNA, which leads to extension of chromatin loops and a less strict segregation between A and B compartments with a decrease of far-*cis* contacts (Haarhuis *et al*, 2017). In contrast to topologically associating domains (TAD) boundaries, which are generally conserved among cell types, A and B compartments are cell type specific (Rao *et al*, 2014; Dixon *et al*, 2015; Bonev *et al*, 2017). However, the mechanisms underlying these changes and their impact on gene expression and epigenetic states remain yet unclear.

Pluripotent embryonic stem cells (ESCs) provide an exceptional system to address this question as they exist in a variety of states that represent distinct chromatin and epigenetic features. *In vitro*, ESC types are largely defined by culture conditions, which mimic the natural development of the embryo from the blastocyst to post-implantation stages (Hackett & Surani, 2014). ESCs can be propagated in medium containing fetal calf serum and leukemia inhibitory factor (LIF; ESC+serum) or in serum-free 2i medium (ESC+2i) that contains LIF plus

1   Department of Molecular Mechanisms of Disease, DMMD, University of Zurich, Zurich, Switzerland
2   Molecular Life Science Program, Life Science Zurich Graduate School, University of Zurich, Zurich, Switzerland
3   Department of Computational Biology, University of Lausanne, Lausanne, Switzerland
4   Service and Support for Science IT, University of Zurich, Zurich, Switzerland
5   Oncode Institute, Hubrecht Institute-KNAW, University Medical Center Utrecht, Utrecht, The Netherlands
    *Corresponding author. Tel: +41 44 63 55475; E-mail: raffaella.santoro@dmmd.uzh.ch

two small-molecule kinase inhibitors for MEK/ERK (PD0325901) and GSK3 (CHIR99021; Ying *et al*, 2008). Both ESC+2i and ESC+serum are pluripotent. ESC+2i closely resemble the developmental ground-state *in vivo* whereas ESC+serum are developmentally advanced (Boroviak *et al*, 2014). These two pluripotent cell types display distinct chromatin and epigenetic features. At the nucleosomal level, the chromatin configuration is more open in ESC+2i than in ESC+serum (Ricci *et al*, 2015). Furthermore, the epigenetic and chromatin organization of ESC+2i is in a less repressed state. ESC+2i have hypomethylated DNA similar to pre-implantation embryos, whereas ESC+serum genome is hypermethylated, reminiscent of post-implantation embryos (Marks *et al*, 2012; Ficz *et al*, 2013; Habibi *et al*, 2013; Leitch *et al*, 2013). Similarly, there is a reduced prevalence of the repressive H3K27me3 mark at Polycomb target promoters in ESC+2i (Marks *et al*, 2012; Joshi *et al*, 2015). Recent studies showed that ESC+serum contain a set of extremely long-range interactions that depend on Polycomb repressive complexes 1 and 2 (PRC1, PRC2; Joshi *et al*, 2015; Schoenfelder *et al*, 2015). In contrast, ESC+2i do not contain these long-range PRC interactions and instead exhibit chromatin decompaction at PRC target loci (Joshi *et al*, 2015; McLaughlin *et al*, 2019).

In this work, we made use of these two closely and developmentally related ESC types to elucidate how genome organization and compartmentalization are regulated according to cell state and chromatin structure. We show that only the active and open genome of ground-state ESCs rely on BAZ2A (also known as TIP5), a factor that together with SNF2H (SMARCA5) constitutes the nucleolar remodeling complex NoRC (Santoro *et al*, 2002). BAZ2A interacts on ESC chromatin with SNF2H, DNA topoisomerase 2A (TOP2A) and cohesin. We found that BAZ2A associates with sub-domains within the active A compartment that strongly intersect through long-range contacts in ESCs. BAZ2A specifically regulates the highly open chromatin of ESC+2i by limiting the invasion of active domains into repressive compartments. Depletion of BAZ2A specifically affects ground-state ESCs by increasing chromatin accessibility at chromatin regions including the repressed B compartments, which in turn decrease their repressive features such as upregulation of gene expression and acquisition of active epigenetic marks. Furthermore, the binding of BAZ2A with active chromatin domains of ground-state ESCs regulates H3K27me3 genome occupancy, a process that also involves TOP2A. Finally, the ground-state-specific role of BAZ2A was also evident by impaired differentiation capacity and deregulation of genes linked to developmental process, which all occur only upon BAZ2A depletion in ESC+2i whereas ESC+serum remained unaffected. Our results suggest that chromatin remodeling and topoisomerase activities might serve to counteract the intrinsic propensity of the highly open and active chromatin of ground-state ESCs to invade repressive domains. This effort in controlling open/active chromatin domains is required to establish active and repressed genome partitioning and preserves cell function and identity.

Results

Ground-state and developmentally advanced pluripotent ESCs differ in the requirement of BAZ2A for cell proliferation and differentiation capacity

The nucleolar remodeling complex NoRC consists of two subunits, the ATPase SNF2H and BAZ2A, a >200 kDa protein that shares

sequence homology with the largest subunits of SNF2H/ISWI-containing remodeling complexes (Strohner *et al*, 2001; Santoro *et al*, 2002). In differentiated cells, BAZ2A is mainly localized in nucleoli, associates with ribosomal RNA (rRNA) genes and establishes their epigenetic silencing (Santoro *et al*, 2002; Mayer *et al*, 2006; Guetg *et al*, 2010). In contrast, in ESCs, recruitment of BAZ2A to rRNA genes, its ability to silence rRNA genes, and its nucleolar localization are impaired through a long non-coding RNA-mediated mechanism (Savic *et al*, 2014; Leone *et al*, 2017).

Our previous work and initial analysis suggested that in ESCs BAZ2A function was not related to rRNA transcriptional control. First, BAZ2A is more highly expressed in ESC+2i than in differentiated cells (Fig 1A). Second, although not bound to rRNA genes, BAZ2A is still tightly associated with chromatin in ESC+2i (Fig 1B). Third, and consistent with previous results (Savic *et al*, 2014), we observed a decrease in cell number of ESC+2i upon BAZ2A depletion by siRNA (Fig 1C and D). Similar results were obtained with a different siRNA and in another ESC line (Appendix Fig S1A and B). BAZ2A downregulation in ESC+2i induced a moderate arrest at G1 phase of cell cycle without any evident sign of apoptotic cell death (Appendix Fig S1C–E). Fourth, and in line with previous results (Savic *et al*, 2014), after induction of monolayer differentiation upon withdrawal of LIF, ESC+2i treated with siRNA-*Baz2a* underwent cell death while control cells displayed morphological structures typical of differentiated cells and were negative for alkaline phosphatase staining (Fig 1F and G). All these results indicated that ground-state ESCs depend on BAZ2A expression for proliferation and differentiation capacity and highlighted an unexpected non-nucleolar function of BAZ2A. Next, we asked whether developmentally advanced ESC+serum were also dependent on BAZ2A. Surprisingly, although BAZ2A expression levels and knockdown efficiency in ESC+2i and ESC+serum were similar (Fig 1C and E), depletion of BAZ2A in ESC+serum did not cause any evident defect in proliferation or differentiation (Fig 1D,F, and G), suggesting ground-state-specific role of BAZ2A. To further support these results, we performed CRISPR/Cas9 to generate *Baz2a*-KO directly in ESC+serum and ESC+2i. While we were able to generate *Baz2a*-KO lines in ESC+serum (Fig 1H), all our attempts to establish *Baz2a*-KO directly in ESC+2i failed, a result that is consistent with the proliferative defects observed upon siRNA-mediated BAZ2A depletion only in ESC+2i, but not in ESC+serum (Fig 1H). Cell morphology, proliferation, and differentiation capacity were similar between control and *Baz2a*-KO ESC+serum (Fig 1I and J, Appendix Fig S1F). However, during the transition from serum to 2i conditions *Baz2a*-KO cells lose self-renewal and proliferation capacity with substantial cell death (Fig 1J, Appendix Fig S1G), indicating that BAZ2A is specifically essential in ground-state ESCs.

Taken together, these results highlighted a substantial difference in the requirement of BAZ2A for cell proliferation and differentiation capacities between ground-state and developmentally advanced pluripotent ESCs.

BAZ2A regulates gene expression in ground-state ESCs

To elucidate the ground-state-specific role of BAZ2A, we analyzed gene expression of ESC+2i and ESC+serum treated with siRNA-*Baz2a* or siRNA-control (Fig 2A, Table EV1). We found that depletion of BAZ2A induces greater differential gene expression in ESC+2i

than in ESC+serum. Upon BAZ2A depletion in ESC+2i, 1934 genes showed transcriptional changes (log$_2$ fold change > 0.58; P<0.05; BAZ2A 2i-regulated genes: 1236 upregulated and 698 downregulated). In contrast, ESC+serum depleted for BAZ2A showed only moderate changes in gene expression compared with ESC+2i, and the total number of genes affected by BAZ2A knockdown was almost four times less (351 upregulated and 207 downregulated; Fig 2A). Only a minority of differentially expressed genes were
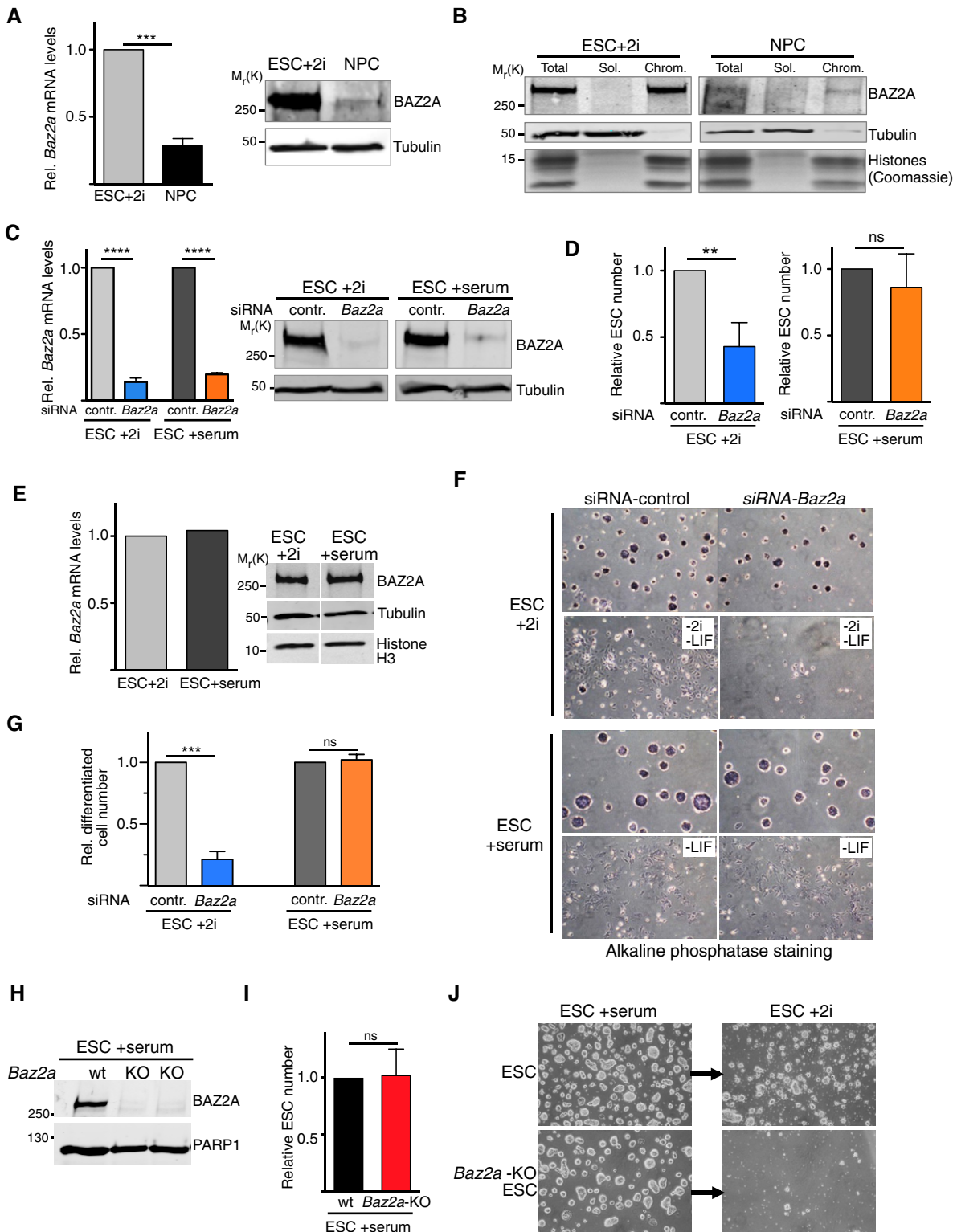

Figure 1.

Figure 1. BAZ2A is required for proliferation and differentiation of ESC+2i.

A   BAZ2A expression is higher in ESC+2i than in differentiated cells (neural progenitors, NPC). Left panel. *BAZ2A* mRNA levels were measured by qRT–PCR and normalized to *Rps12* mRNA and to ESC+2i. Average values of three independent experiments. Error bars represent s.d., and statistical significance (*P*-values) was calculated using the paired two-tailed *t*-test (*** < 0.001). Right panel. Western blot showing BAZ2A protein levels in ESC+2i and NPC. Tubulin is shown as a protein loading control.

B   BAZ2A associates with chromatin of ESC and NPC. Chromatin-bound (Chrom.) and soluble (Sol.) fractions of equivalent cell number of ESC+2i and NPCs were analyzed by Western blot for BAZ2A levels. Total, total protein. Tubulin and histones are shown as loading and fractionation control.

C   siRNA-knockdown efficiency of BAZ2A shown by qRT–PCR and Western blot. *BAZ2A* mRNA levels were measured by qRT–PCR and normalized to *Rps12* mRNA and to each ESC line. Average values of three independent experiments. Error bars represent s.d. and statistical significance (*P*-values) was calculated using the paired two-tailed *t*-test (**** < 0.0001). Right panel. Western blot showing BAZ2A protein levels. Tubulin is shown as a protein loading control.

D   BAZ2A knockdown affects proliferation of ESC+2i but not of ESC+serum. Data represent relative cell numbers after 3 days of siRNA treatment and were normalized to ESC transfected with siRNA-Control. Average values of three independent experiments. Error bars represent s.d. Statistical significance (*P*-values) for the experiments was calculated using the paired two-tailed *t*-test (** < 0.01; ns, non-significant).

E   BAZ2A is expressed at similar levels in both ESC+2i and ESC+serum. Left panel. *BAZ2A* mRNA levels were measured by qRT–PCR and normalized to *Rps12* mRNA and to ESC+2i. Average values of three independent experiments. Error bars represent s.d. Right panel. Western blot showing BAZ2A protein levels in ESC+2i and ESC+serum. Tubulin and histone H3 are shown as a protein loading controls.

F   BAZ2A is required for the differentiation of ESC+2i but not for ESC+serum. Representative images of alkaline phosphatase staining of ESC and cells after 3 days of differentiation upon culture in completed medium containing 10% serum and in the absence of LIF.

G   Quantification of differentiated cells. Values represent relative number of differentiated cells from three independent experiments relative to control cells. Error bars represent s.d. Statistical significance (*P*-values) for the experiments was calculated using the paired two-tailed *t*-test (*** < 0.001; ns, non-significant).

H   Western blot showing BAZ2A protein levels in two BAZ2A-KO ESC lines obtained via CRISPr/Cas9 directly in ESC+serum. PARP1 is shown as a protein loading control.

I   Cell proliferation is not affected in BAZ2A-KO ESC+serum. Data represent relative cell numbers 2 days culture starting with the same number of cells. Average values of four independent experiments. Error bars represent s.d. Statistical significance (*P*-values) for the experiments was calculated using the paired two-tailed *t*-test (ns, non-significant).

J   Representative images of wt and *Baz2a*-KO ESC+serum before and after transition in 2i conditions.

upregulated (65) or downregulated (56) by BAZ2A knockdown in both ESC states (Fig EV1A). Validation by qRT–PCR, using two siRNAs and a different ESC line, supported a role of BAZ2A in the regulation of gene expression in ESC+2i but not in ESC+serum (Figs 2B and EV1B and C). Gene ontology analysis revealed that differentially expressed genes in ESC+2i are enriched in pathways linked to developmental processes (Fig 2C, Table EV2). In contrast, genes differentially expressed in ESC+serum were mostly implicated in biological processes linked to cell signaling and cell adhesion.

Next, we asked whether the role of BAZ2A in the regulation of gene expression specifically in ESC+2i was a consequence of the chromatin state of these cells (low DNA methylation and low H3K27me3 occupancy at PRC target promoters). To mimic this status in ESC+serum, we analyzed ESCs that lack DNA methyltransferases DNMT1, 3B, and 3A (TKO-ESC) or the core components of PRC1 and PRC2 complexes (Ring1b$^{-/-}$ ESC and Eed$^{-/-}$ ESC). BAZ2A depletion in these ESC-KO lines cultured in serum did not affect cell proliferation or expression of BAZ2A 2i-regulated genes (Fig EV1D–G). These results show that BAZ2A specifically affects gene expression of ESC+2i and suggest that this process might not depend on the low DNA methylation content and low H3K27me3 levels at PRC target promoters characterizing ground-state ESCs.

BAZ2A associates with large and active genomic regions of ESCs

To determine how BAZ2A specifically regulates gene expression in ground-state ESCs, we measured and compared BAZ2A genomic occupancy between ESC+2i and ESC+serum. We established an ESC line containing a FLAG-HA (F/H) tag at the N-terminus of both *Baz2a* alleles (Appendix Fig S3A–C). Previous studies showed that the fusion of the F/H peptide at the N-terminus of BAZ2A does not affect its activity (Mayer *et al*, 2006; Guetg *et al*, 2012). The obtained ESC lines (F/H-BAZ2A-ESC) express BAZ2A at levels similar to wild-type (wt) cells (Fig 3A). Furthermore, cell morphology, proliferation, and expression of pluripotency genes were similar in

both F/H-BAZ2A-ESC and parental ESC. We performed ChIP-seq analysis with anti-FLAG or anti-HA immunoprecipitation and assessed the specificity of BAZ2A-ChIP by comparing FLAG- or HA-ChIP of F/H-BAZ2A-ESCs and wt-ESCs. ChIP results were consistent with previous data showing a lack of BAZ2A association with rRNA genes in both ESC+2i and ESC+serum (Fig 3B; Savic *et al*, 2014). The genomic binding pattern of BAZ2A in both ESC+2i and ESC+serum did not appear as a distinct peak-like profile typical of transcription factors, but was rather enriched over large domains that extended up to several hundred kb (average size 33 kb, Fig 3C). In contrast to differentiated cells, where BAZ2A associates with repressive epigenetic signatures (i.e., DNA methylation and K3K9me2/3; Santoro *et al*, 2002), we found that BAZ2A occupies active regions of the genome marked by H3K4me1 and H3K27ac and its occupancy correlates poorly with the repressive marks H3K27me3 and H3K9me3 levels in ESC+2i (Fig 3C and D). Consistently, BAZ2A-bound regions were predominantly excluded from the repressed lamina-associated domains (LADs; Peric-Hupkes *et al*, 2010; Fig EV2A). While genomic distribution was similar in ESC+serum and ESC+2i (>88% commonly bound region; Fig EV2B), the amount of BAZ2A binding was higher in ESC+2i (Fig 3B,C, and E). We validated the levels of BAZ2A binding at selected genomic regions of ESC+2i and ESC+serum by ChIP experiments followed by quantitative (q)PCR measurements (Fig 3B). In total, we found 1263 BAZ2A-bound regions that were unique to either of the two ESC states. Most of ESC state-specific BAZ2A-bound regions were found in ESC+2i (1003 BAZ2A 2i-specific sites, 80% of all unique BAZ2A-bound regions). The lack of BAZ2A binding at these regions in ESC+serum associates with a decrease in H3K27ac or an increase in H3K27me3 content compared with ESC+2i, indicating that the association of BAZ2A with ESC chromatin might depend on an active chromatin signature (Fig 3F and G). These results are also consistent with the reduced BAZ2A binding with the chromatin of ESC+serum that have a more repressed chromatin state compared to ESC+2i. Collectively, these results indicate that BAZ2A associates
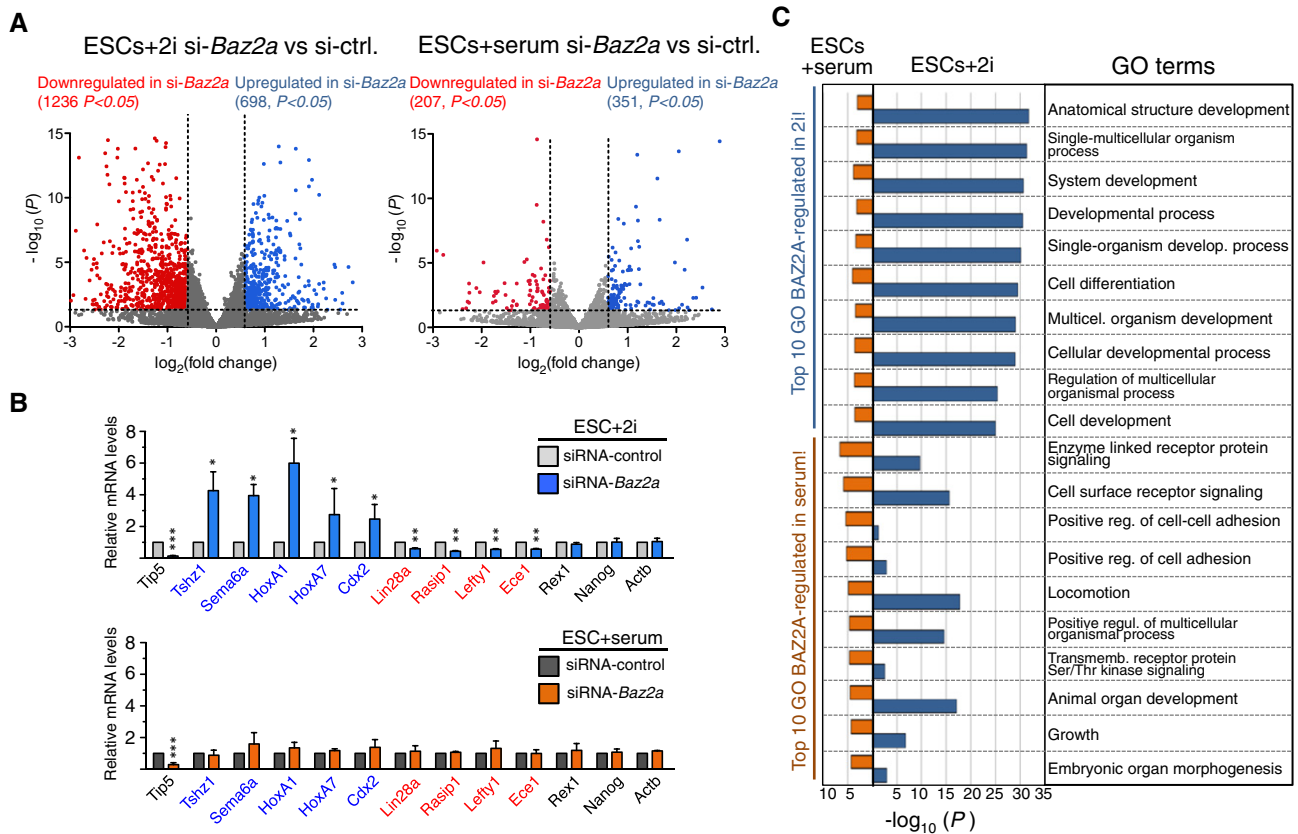
Figure 2. BAZ2A regulates gene expression specifically in ESC+2i.

A Volcano plot showing fold change ($\log_2$ values) in transcript level of ESC+2i and ESC+serum with two consecutive treatments with siRNA-control and siRNA-*Baz2a*, each one lasting for 4 days. Gene expression values of three replicates were averaged and selected for 1.5 fold changes and $P < 0.05$. Statistical significance (P-values) was calculated using R package DEseq2.

B Validation by qRT–PCR of genes regulated by BAZ2A in ESC+2i but not in ESC+serum (upregulated genes in ESC+2i upon BAZ2A-KD are labeled in blue, downregulated genes are in red). *Nanog*, *Rex1*, and *Actin* B (*ActB*) are shown as genes not regulated by BAZ2A. mRNA levels were normalized to *Rps12* mRNA and to ESCs transfected with siRNA-Control. Average values of three independent experiments. Error bars represent s.d. Statistical significance (P-values) for the experiments was calculated using the paired two-tailed t-test (* < 0.05, ** < 0.01, *** < 0.001). Data without P-values are statistically non significant.

C Top 10 biological process gene ontology terms as determined using DAVID for genes regulated by BAZ2A in ESC+2i and ESC+serum.

with large and active chromatin domains, which are characterized by high H3K27ac and low H3K27me3 contents. Furthermore, despite the specific dependency of ESC+2i on BAZ2A for gene expression, proliferation, and differentiation capacity, BAZ2A genomic occupancy is similar in these two ESC types.

To gain insights on how BAZ2A binding impacts gene expression, we investigated the position of BAZ2A-bound sites relative to differentially expressed genes in ESC+2i. Surprisingly, we found that BAZ2A-bound regions in ESC+2i, including BAZ2A 2i-specific sites, were depleted in the vicinity of BAZ2A 2i-regulated genes ($\log_2$(-fold) $= -0.77$, FDR 10^{-4}; Figs 3H and EV2C). Moreover, we did not observe any evident positive correlation for linear genomic distance between BAZ2A-bound enhancers and BAZ2A 2i-regulated genes (Fig EV2D and E). These results are also consistent with ChIP-seq analyses showing that BAZ2A 2i-regulated genes were enriched for H3K27me3 and depleted in H3K27ac (Fig 3I and J), a chromatin signature that anticorrelates with the active chromatin regions bound by BAZ2A (Fig 3C, D, and F). We conclude that the gene expression changes associated with BAZ2A in ESC+2i are not a

consequence of the direct binding of BAZ2A to cis-acting regulatory elements (promoters and enhancers) of BAZ2A-2i regulated genes.

BAZ2A-bound regions mark highly interacting long-range contacts in ESCs

Since BAZ2A binds large active chromatin domains that are distal to the cis-regulatory elements of genes regulated by BAZ2A in ESC+2i, we analyzed BAZ2A occupancy relative to the 3D genome organization of ESCs. First, we made use of recently published high resolution (<750 bp) Hi-C map in ESC+serum, the highest to date in mammalian cells (Bonev *et al*, 2017). Consistent with BAZ2A binding to regions enriched in active histone modifications, we found that 96% of BAZ2A-bound regions are found in the active A compartment (Fig 4A). Strikingly, we found stronger far-*cis* contacts between BAZ2A-bound regions in the genome, in general, and within A compartment, in particular, compared with near-*cis* contacts and interactions of regions not bound by BAZ2A genome wide (Fig 4B and C). These long-range contacts marked by BAZ2A
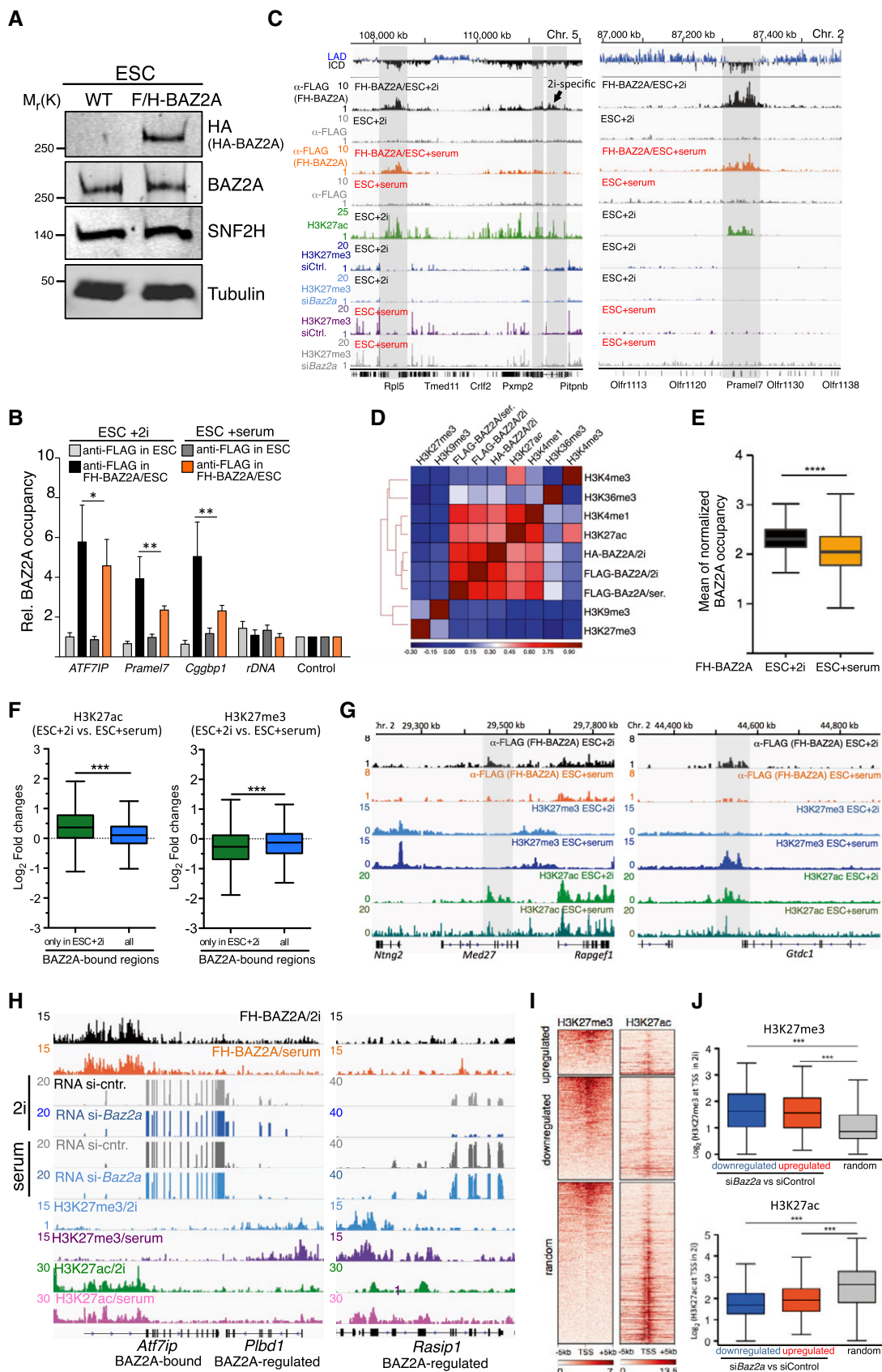
Figure 3.

◀

Figure 3. BAZ2A associates with large and active chromatin domains in ESCs.

A Western blot showing equal BAZ2A levels in wt-ESC and F/H-BAZ2A ESC line containing FLAG-HA sequences at the N-terminus of both *Baz2a* alleles. Whole cell lysates from equivalent amounts of cells were analyzed. SNF2H and Tubulin are shown as protein loading controls.

B Anti-FLAG ChIP of wt-ESCs and F/H-BAZ2A-ESCs cultured in 2i or serum. Data were measured by qPCR and normalized to input and a control region that is not bound by BAZ2A. Average values of three independent experiments. Error bars represent s.d., and statistical significance (P-values) was calculated using the paired two-tailed *t*-test (* < 0.05, ** < 0.01).

C Representative images showing the association of BAZ2A at regions enriched in H3K27ac and low in H3K27me3. The gray rectangles highlighted some of BAZ2A associated regions.

D Pearson's correlation heat map for the indicated ChIP-seqs in ESC+2i. BAZ2A ChIP-seqs were performed with FLAG antibodies in *F/H*-BAZ2A-ESCs cultured in 2i or serum and with HA antibodies in *F/H*-BAZ2A-ESC+2i. Data of H3K4me3, H3K27ac, and H3K27me3 are from this work. H3K36me3, H3K9me3, and H3K4me1 values in ESC+2i were taken from published data sets (Marks *et al*, 2012; Joshi *et al*, 2015).

E Box plot showing the mean of normalized BAZ2A occupancies in ESC+2i and ESC+serum at BAZ2A-bound regions. Statistical significance (P-values) for the experiments was calculated using the unpaired two-tailed *t*-test (**** < 0.0001). Box plots depict the minimum and maximum values. The mean is represented by a horizontal line within the boxes.

F Differential BAZ2A-binding in 2i and serum correlates with H3K27ac occupancies. Box plot showing the mean of normalized H3K27ac and H3K27me3 read counts in ESC+2i and ESC+serum at all BAZ2A-bound regions and BAZ2A-bound regions only in 2i were calculated and their log2-fold changes are plotted. H3K27ac in ESC+serum were taken from (Joshi *et al*, 2015). Statistical significance (P-values) was calculated using the paired two-tailed *t*-test (*** < 0.001). Box plots depict the minimum and maximum values. The mean is represented by a horizontal line within the boxes.

G Representative images showing 2i-specific BAZ2A-bound regions and H3K27ac and H3K27me3 in ESC+2i and ESC+serum. The gray box highlights strong TIP5-bound regions and corresponding histone modifications.

H Representative images showing that genes regulated by BAZ2A are enriched in H3K27me3, depleted of H3K27ac and not bound by BAZ2A.

I Heat map profiles of H3K27me3 and H3K27ac at ±5 kb from the TSS of genes differentially regulated by BAZ2A in ESC+2i and random genes. Differentially regulated genes are shown as upregulated or downregulated in ESC+2i upon BAZ2A knockdown. Data were ranked by H3K27me3 levels. Transcription start site (TSS).

J Box plot showing the mean of normalized H3K27me3 and H3K27ac read counts over ±1 kb of TSSs from upregulated, downregulated, and random genes. Box plots depict the minimum and maximum values. The mean is represented by a horizontal line within the boxes.

binding are specific to ESCs as they were gradually lost during the progression of neural differentiation (neural progenitors, NPCs, and cortical neurons, CNs; Figs 4D and EV2F).

Given the differences between BAZ2A function in ESC+serum and ESC+2i, we next performed Hi-C analysis of ESC+2i (three independent biological experiments, 95 million pair end reads). Despite the relative lower resolution of these Hi-C maps relative to the Hi-C data of ESC+serum (Bonev *et al*, 2017), the conclusions of the analysis of both data sets were similar. A and B compartments annotated in ESC+2i (our Hi-C) and in ESC+serum (Hi-C from Bonev *et al* (2017)) were well correlated, indicating that despite the differences in chromatin states between the two ESC types genome compartmentalization is similar (Fig EV2G). Moreover, ESC+2i and ESC+serum showed a similar contact profile, including higher far-*cis* contacts at A compartments compared with near-*cis* contacts, which is consistent with previous results showing the propensity of active chromatin of ESCs to segregate and establish long-range interactions (Bonev *et al*, 2017; Fig EV2H). We found that BAZ2A-bound regions in ESC+2i are also found within A compartments (Fig 4E). Consistent with our analysis in ESC+serum, also in ESC+2i, far-*cis* contacts between BAZ2A-bound regions are the strongest relative to near-*cis* contacts and between regions not bound by BAZ2A (Figs 4F and EV2I). Therefore, although chromatin is more open and epigenetically active in ESC+2i than in ESC+serum, genome compartmentalization and BAZ2A-bound far-*cis* contacts are similar in both ESC types.

BAZ2A-bound regions within the A compartment of ESC+2i and ESC+serum had higher eigenvector values than regions not bound by BAZ2A (Fig EV2J). Remarkably, the correlation between ChIP-seq signal enrichment for BAZ2A binding and histone marks and eigenvector value indicated that BAZ2A has the strongest correlation with positive eigenvector values in both ESC+2i and ESC+serum (Fig 4G). The presence of A and B sub-compartments with distinct patterns of histone modifications has been described in human differentiated cells (Rao *et al*, 2014). As BAZ2A associates with H3K27ac and H3K4me1 domains (Fig 3D), these A

subcompartments represent regions particularly enriched in active histone marks. Strikingly, however, the strength in far-*cis* contacts between BAZ2A-bound regions and regions not bound by BAZ2A does not depend on H3K27ac and H3K4me1 levels (Fig 4H). Taken together, the results indicate that BAZ2A associates with subdomains within the active A compartment that strongly intersect through long-range contacts in ESCs.

BAZ2A counteracts the propensity of active chromatin of ground-state ESCs to invade repressive domains

The binding of BAZ2A within active chromatin regions engaged in long-range contacts in ESCs, suggested to us that BAZ2A could impact chromatin states and contribute to gene expression specifically in ground-state but not developmentally advanced ESCs. To test this, we first measured chromatin accessibility upon BAZ2A knockdown in both ESC types using ATAC-seq. As expected, the most accessible chromatin regions in both ESC types were found in A compartments (72% in ESC+2i, 75% in ESC+serum; Figs 5A and EV3A). About one-third of accessible chromatin sites coincided with BAZ2A bound regions, supporting the previous analyses showing that BAZ2A associates with active chromatin regions that are known to have elevated chromatin accessibility (Fig EV3B). ESC+2i displayed higher chromatin accessibility in B compartment compared with ESC+serum, underscoring the more open chromatin state of ESC+2i even at repressive domains (Fig 5B and C). Increased chromatin accessibility correlates with elevated H3K27ac levels in both ESC types, indicating that this modification specifically marks distinct open chromatin domains in the two pluripotency states (Fig 5D). Remarkably, depletion of BAZ2A induced changes in chromatin accessibility of ESC+2i whereas ESC+serum were unaffected, indicating that BAZ2A specifically modulates chromatin structure in ground-state ESCs (Figs 5E and F and EV3C). Overall, BAZ2A knockdown increased chromatin accessibility in ESC+2i (1952 increased chromatin accessibility sites vs. 440
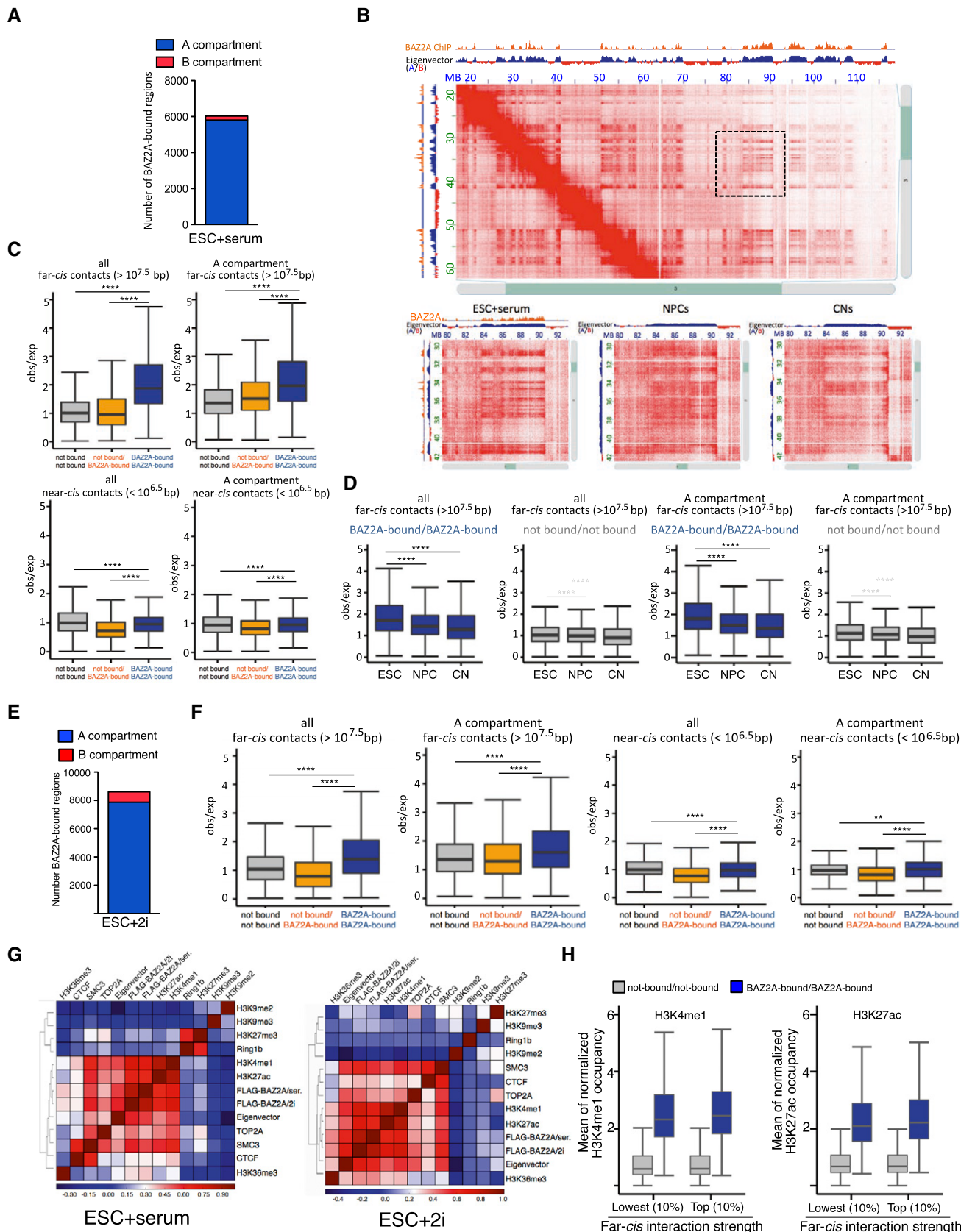
Figure 4.

Figure 4. BAZ2A-bound regions mark the highly interacting long-distance contacts in ESCs..

A   Number of BAZ2A-bound regions in A and B compartments of ESC+serum.

B   Hi-C contact matrices for a zoomed in region on chromosome 3 at 100-kb resolution showing the presence of strong long-distance contacts corresponding to regions in A compartment bound by BAZ2A in ESC+serum. Low panels. Hi-C contacts of a zoomed region at 50-kb resolution in ESC+serum, NPCs, and CNs are shown. Data are from (Bonev *et al*, 2017). Hi-C contacts were visualized using Juicebox (Rao *et al*, 2014).

C   BAZ2A-bound regions mark A subcompartments that are characterized by the strongest far-*cis* contacts in ESC+serum. Box plots indicating observed/expected contact values between BAZ2A-bound regions and loci not bound by BAZ2A at near-*cis* and far-*cis* contacts in all genome or in A compartments. Statistical significance (*P*-values) was calculated using the unpaired two-tailed *t*-test (**** < 0.0001).

D   Long-range contacts marked by BAZ2A binding are specific for ESCs. Box plots indicating observed/expected contact values between BAZ2A-bound regions and loci not bound by BAZ2A at far-*cis* contacts in all genome or in A compartments of ESC+serum, NPC and CN. Statistical significance (*P*-values) was calculated using the unpaired two-tailed *t*-test (**** < 0.0001). Box plots depict the minimum and maximum values. The mean is represented by a horizontal line within the boxes.

E   Number of BAZ2A-bound regions in A and B compartments in ESC+2i.

F   BAZ2A-bound regions mark A subcompartments that are characterized by the strongest far-*cis* contacts in ESC+2i. Box plots indicating observed/expected contact values between BAZ2A-bound regions and loci not bound by BAZ2A at near-*cis* and far-*cis* contacts in all genome or in A compartments of ESC+2i. Statistical significance (*P*-values) was calculated using the unpaired two-tailed *t*-test (** < 0.001, **** < 0.0001). Box plots depict the minimum and maximum values. The mean is represented by a horizontal line within the boxes.

G   BAZ2A binding correlates the best with eigenvector values. Heat map showing Pearson's correlation values of ChIP-seq data sets with the eigenvector values from Hi-C data in ESC+serum (Bonev *et al*, 2017) and ESC+2i, respectively.

H   Box plots showing H3K4me1 and H3K27ac content of BAZ2A-bound regions and loci not bound by BAZ2A at far-*cis* contacts in ESC+2i. Data from regions with lowest 10% and top 10% contact strength are shown. Box plots depict the minimum and maximum values. The mean is represented by a horizontal line within the boxes.

decreased accessibility sites; Fig 5E and F). Decreased accessibility sites (DAS) were close to genes downregulated upon BAZ2A knockdown, indicating reduced chromatin accessibility at genes that undergo transcriptional repression in the absence of BAZ2A whereas no correlation was found in increased accessibility sites (IAS; Fig 5G). A large portion of DAS (29.28%) was located at gene promoters whereas only 2.94% of IAS were present at these genomic elements (Fig 5H). Almost half (44%) of IAS were located within the B compartment, which is not bound by BAZ2A (Fig 5E). We did not find enrichment in IAS or DAS at BAZ2A-bound regions, indicating that changes in chromatin accessibility upon BAZ2A-KD are not dependent on the direct interaction of BAZ2A with these regions (Fig EV3D). Remarkably, the position of IAS was not homogenously distributed within the compartments (Fig 5I, Table EV3). In B compartments, IAS were only enriched at B boundaries whereas DAS did not show any specific positional enrichment in the A compartment (Fig 5I, Table EV3). Furthermore, we found that also genes upregulated upon BAZ2A depletion in ESC+2i were enriched in B compartment, particularly at B boundaries, relative to all expressed genes (Fig 5I and J, Table EV3). Also in this case, upregulated genes upon BAZ2A-KD in ESC+2i were depleted of BAZ2A-bound sites (Table EV3). Consistent with the increased chromatin accessibility and upregulation of gene expression in B compartment upon BAZ2A depletion, we found that H3K27ac and H3K4me3 levels also increase in B compartments (Fig 5K).

Taken together these results indicated that BAZ2A regulates chromatin accessibility specifically in ESC+2i. Specifically, our data highlighted the role of BAZ2A in limiting invasion of active chromatin into the repressive chromatin of B compartment of ESC+2i.

BAZ2A loss affects 3D genome architecture of ground-state ESCs

To determine whether BAZ2A loss affects genome organization of ground-state ESCs, we performed Hi-C analysis of ESC+2i in control and BAZ2A-depleted ESC+2i. For each group, we performed three independent biological experiments that showed high similarity (Fig EV3E, Table EV4). Analysis of ESC+2i depleted of BAZ2A revealed a genome-wide increase in far-*cis* contacts (>10 Mb) compared with control cells (Figs 6A and B and EV3F). Although these extremely

long-range interactions occurred at a relatively low frequency, their increase upon BAZ2A-KD is consistent across all three independent Hi-C experiments, suggesting that the lack of BAZ2A induced the formation of spurious genomic contacts, a result that might reflect an increase in chromosome flexibility (Haarhuis *et al*, 2017). Increase in long-distance contacts could be observed in both A and B compartments and at BAZ2A-bound regions and regions not bound by BAZ2A (Fig EV3G), a result that is consistent with the expansion of active chromatin, which in ESCs has been shown to be prone to form long-range contacts (Bonev *et al*, 2017). Alterations in genome architecture mediated by BAZ2A depletion in ESC+2i were also evident by a decrease in absolute eigenvector values at the boundaries of B compartments whereas the center regions of B compartment and the entire A compartment were not significantly affected (Fig 6C). These results are consistent with the increased chromatin accessibility and euchromatic histone marks observed close to A and B boundaries upon BAZ2A depletion (Fig 5I and K). Collectively, the results further support a role of BAZ2A in protecting repressive compartments by the invasion of active domains.

BAZ2A regulates H3K27me3 occupancy in ground-state ESCs

To investigate whether BAZ2A might impact the epigenetic landscape at repressed chromatin regions in ESC+2i, we analyzed H3K27me3 that is enriched at Polycomb domains. These regions are often flanked by CTCF boundaries, however, insulation mediated by CTCF does not act as a direct barrier to H3K27me3 spreading (Dowen *et al*, 2014; Nora *et al*, 2017). Western blot analyses indicated that total levels of H3K27me3 are not altered in the absence of BAZ2A (Fig 7A). Strikingly, ChIP-seq experiments revealed a global re-distribution of H3K27me3 in ESC+2i whereas ESC+serum were not affected (Fig 7B and C). For promoters with high levels of H3K27me3, BAZ2A depletion resulted in a decrease in H3K27me3, while promoters with relatively low H3K27me3 levels displayed an increase of this repressive mark (Fig 7B and D). Quantitative H3K27me3 ChIP-seq using *Drosophila* spike-in chromatin and ChIP-qPCR experiments validated the decrease of H3K27me3 at TSS of selected genes with high H3K27me3 content and showed that this effect was specific for ESC+2i (Figs 7E and EV4B). Similar results were also obtained with a

different siRNA-*Baz2a* sequence (Fig EV4C). Importantly, the redistribution of H3K27me3 did not correlate with transcriptional changes observed upon BAZ2A knockdown as both upregulated and downregulated genes showed decreased H3K27me3 occupancies, a result that is consistent with the elevated H3K27me3 content at TSS of BAZ2A 2i-regulated genes (Fig 7F). Furthermore, the changes in H3K27me3 could not account for the transcriptional changes since BAZ2A depletion in *Ring1b*$^{-/-}$ ESCs and *Eed*$^{-/-}$ ESCs cultured in 2i

still affected cell proliferation and expression of BAZ2A-2i-regulated genes (Fig EV4D and E). These results suggest that H3K27me3 alterations in BAZ2A depleted ESC+2i could not be caused by a response to transcriptional differences. Accordingly, alterations in H3K27me3 occupancy was not restricted to TSSs but was also detected at intergenic regions as in the case of a subset of regions where CTCF sites mark transitions in H3K27me3 enrichment (Fig 7G). Upon BAZ2A depletion, H3K27me3 redistributed over CTCF sites, decreasing at
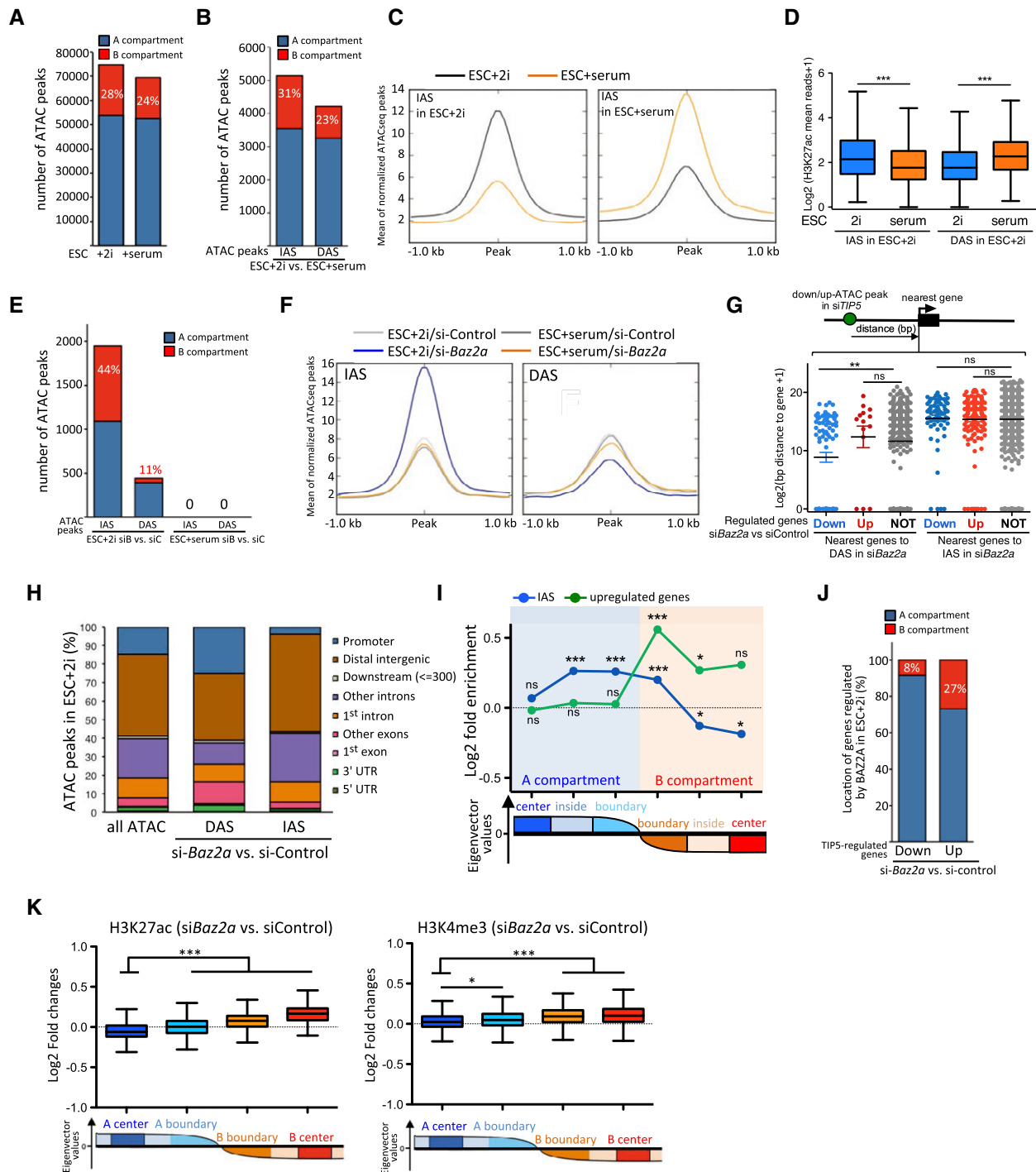

Figure 5.

high H3K27me3 regions and increasing at adjacent low H3K27me3 regions. Consistent with the specific role of BAZ2A in ESC+2i, H3K27me3 transitions marked by CTCF sites in ESC+serum were not affected upon BAZ2A knockdown. These results were validated with independent H3K27me3 ChIP-qPCR experiments and another siRNA-*Baz2a* sequence (Figs 7H and EV4C).

Given that the disruption of boundaries by CTCF depletion was shown not to cause H3K27me3 spreading (Nora *et al*, 2017; Rao *et al*, 2017), the results suggest that alterations in H3K27me3 content might occur through changes in genome organization mediated by BAZ2A loss. To test this, we analyzed the H3K27me3 domain *HoxA* gene cluster that is not bound by BAZ2A and shows strong internal contacts in ESC+2i, forming a small sub-compartment that separates two larger TADs (Fig 7I). Upon BAZ2A depletion, this domain decreased H3K27me3 content and displayed alterations in contacts. Noteworthy, new contacts formed between the *HoxA* cluster and active domains previously bound by BAZ2A and *HoxA1* and *HoxA7* genes became upregulated (Fig 2B, Table EV5). Structural changes were also observed at another H3K27me3 domain, the *HoxB* locus, showing loss of loop anchor points and fusion with the adjacent compartment (Fig EV4F). Together, these results indicate that BAZ2A regulates H3K27me3 occupancy specifically in ESC+2i. Alterations in H3K27me3 are not a direct consequence of transcriptional changes or BAZ2A binding with these regions but instead are likely a consequence of the lack of BAZ2A binding within active chromatin domains that affects genome organization.

TOP2A interacts with BAZ2A and its activity is required for BAZ2A function

In order to understand how BAZ2A affects genome organization and chromatin features in ESC+2i, we analyzed which proteins interact with BAZ2A. Due to its tight association with chromatin, we aimed to purify BAZ2A and its direct interaction partners in their native environment by establishing a protocol that allows immunoprecipitation from purified chromatin (Chromatin IP, Fig 8A). F/H-BAZ2A and wt-ESC nuclei were incubated with the reversible protein–protein specific cross-linker dithiobis(succinimidyl propionate; DSP), and chromatin was isolated by centrifugation of nuclear extracts. After digestion with MNase, solubilization of mononucleosomes was achieved with 1% SDS, which does not affect protein–protein interactions stabilized by DSP cross-linking. The identification of BAZ2A-interacting proteins on chromatin was determined by comparing anti-FLAG immunoprecipitates from F/H-BAZ2A and wt-ESC chromatin followed by mass spectrometry (Fig 8B). Analysis from three independent experiments revealed 24 proteins that consistently interact with BAZ2A in ESC+2i. As expected, the strongest interacting partner of BAZ2A was SNF2H (Fig 8B), suggesting that the function of BAZ2A in ESCs can be directed via the remodeling complex NoRC. Moreover, we detected all known and previously validated BAZ2A-interactors in differentiated cells such as DNMT1, PARP1, and DHX9 (Strohner *et al*, 2001; Santoro *et al*, 2002; Guetg *et al*, 2012; Leone *et al*, 2017). Remarkably, among the top BAZ2A-interacting proteins, we found Topoisomerase 2A (TOP2A) and structural maintenance of chromosomes protein 3 (SMC3), which is part of the cohesin complex (Fig 8B and C). Furthermore, two out of three chromatin IP experiments detected the interaction of BAZ2A with another cohesin component, SMC1 (Table EV6). Western blot analysis validated these results and revealed that BAZ2A interacts with TOP2A and cohesin in both ESC+2i and ESC+serum. Importantly, in the correlation analysis between ChIP-seq signal enrichment and eigenvector values in ESCs, TOP2A and cohesin cluster together and were close to BAZ2A and eigenvector
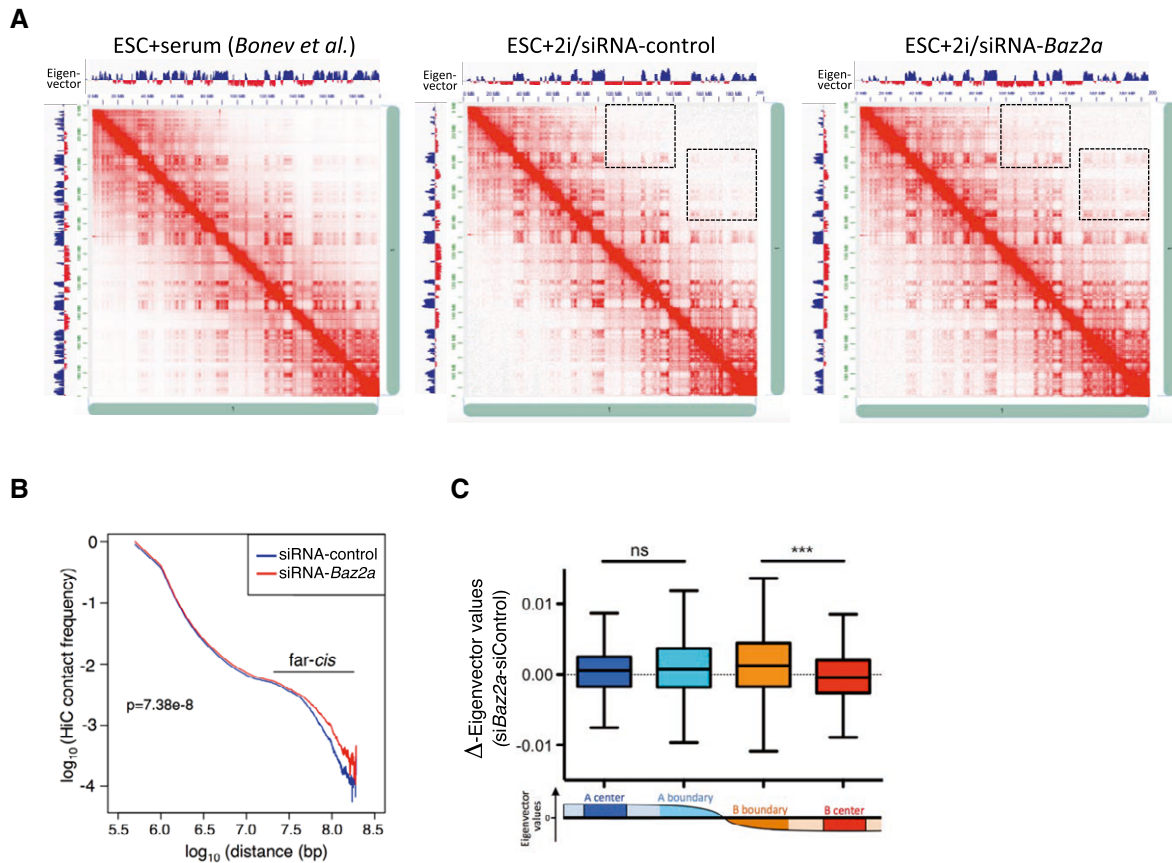
A — ESC+serum (*Bonev et al.*) — ESC+2i/siRNA-control — ESC+2i/siRNA-*Baz2a*

Figure 6. BAZ2A limits spurious long-distant contacts in ground-state ESCs.

A Hi-C contact matrices for chromosome 1 of ESC+serum, ESC+2i/siRNA-control, and ESC+2i/siRNA-*Baz2a* showing the presence of strong long-distance contacts corresponding to regions in A compartment bound by BAZ2A in ESC+serum. Cells were subjected to two consecutive treatments with siRNA-control and siRNA-*Baz2a*, each one lasting for 4 days. Eigenvector values are shown. Increase in far-*cis* contacts in ESC+2i upon BAZ2A-KD is highlighted with a rectangle.

B Relative contact frequencies over genomic distances in ESCs treated with siRNA-control and siRNA-BAZ2A. Statistical significance (*P*-values) was calculated using the Kolmogorov–Smirnov test.

C Box plot indicating differences in eigenvector values at boundaries and centers of A and B compartments. Differences in eigenvector values were calculated from Hi-C data sets from ESC+2i treated with siRNA-*Baz2a* and siRNA-control. Statistical significance (*P*-values) for the experiments was calculated using the unpaired two-tailed *t*-test (*** < 0.001, ns: non-significant). Box plots depict the minimum and maximum values. The mean is represented by a horizontal line within the boxes.

values (Fig 4G). Both TOP2A and cohesin are well known regulators of chromatin architecture. Topoisomerases exert the key function in relieving torsional stress of DNA (Nitiss, 2009). In ESCs, TOP2A is the most highly expressed type II isoenzyme and its inactivation is embryonically lethal (Akimitsu *et al*, 2003; Tiwari *et al*, 2012). We did not detect any interaction of BAZ2A with CTCF, a result that is consistent with the lack of BAZ2A enrichment at TAD boundaries and CTCF sites. Interestingly, recent results revealed that abolishing cohesin loading to DNA resulted in an increase of far-*cis* chromatin contacts as we observed upon BAZ2A depletion in ESC+2i (Haarhuis *et al*, 2017).

To determine whether TOP2A regulates ESC+2i similarly to BAZ2A, we analyzed and compared gene expression in ESC+2i and ESC+serum upon knockdown of TOP2A or after treatment with ICRF-193, a potent TOP2 inhibitor (Pommier *et al*, 2010). Depletion of TOP2A or treatment with ICRF-193 in ESC+2i induced transcriptional changes at candidate genes that mimicked those observed upon BAZ2A knockdown (Fig 8D and E). Moreover, the lack of

apparent additive activation or repression of BAZ2A 2i-regulated genes upon combined depletion suggests that BAZ2A regulates gene expression in ESC+2i with TOP2A via shared pathways. Importantly, depletion of TOP2A or treatment with ICRF-193 in ESC+serum had either a moderate effect (*HoxA1* and *Lefty1*) or no effect in gene expression of the analyzed BAZ2A 2i-regulated genes. Finally, H3K27me3 changes upon TOP2A depletion were similar to those observed upon BAZ2A knockdown (Fig 8F). Also in this case, alterations in H3K27me3 were observed only in ESC+2i but not in ESC+serum.

Depletion of cohesin component SMC3 in ESC+2i caused similar changes in gene expression of BAZ2A 2i-regulated genes (Fig EV5A). In ESC+serum, however, SMC3 depletion could still induce activation of *Sema6a* and only a moderate upregulation of *HoxA7*. As in the case of BAZ2A, upregulated genes upon SMC3-KD in ESC+2i were depleted of cohesin-bound sites (Table EV3). Interestingly, in both ESCs depleted of SMC3, BAZ2A levels were reduced at both protein and mRNA levels (Fig EV5A and B).

Although the reduction in BAZ2A might have an influence on the analysis of BAZ2A 2i-regulated genes by SMC3 depletion in ESC+2i, this decrease was not sufficient to affect H3K27me3 occupancy since upon SMC3 knockdown H3K27me3 levels remain the same, a result that is consistent with previous studies (Rao *et al*, 2017; Fig EV5C).

To determine how TOP2A and SMC3 act together with BAZ2A, we analyzed whether they are required for the association of BAZ2A with chromatin. We performed BAZ2A-ChIP analyses in ESC+2i and

ESC+serum and found that TOP2A depletion as well as inhibition of topoisomerase activity decreased the association of BAZ2A with BAZ2A-bound sequences in both ESC+2i and ESC+serum (Fig EV5D–E). SMC3 depletion reduced the association of BAZ2A with chromatin in ESC+2i whereas this effect was relatively modest in ESC+serum (Fig EV5F). However, we cannot exclude that the lower association of BAZ2A with target genes in ESC+serum might make an eventual reduction of BAZ2A binding in ESC+serum not
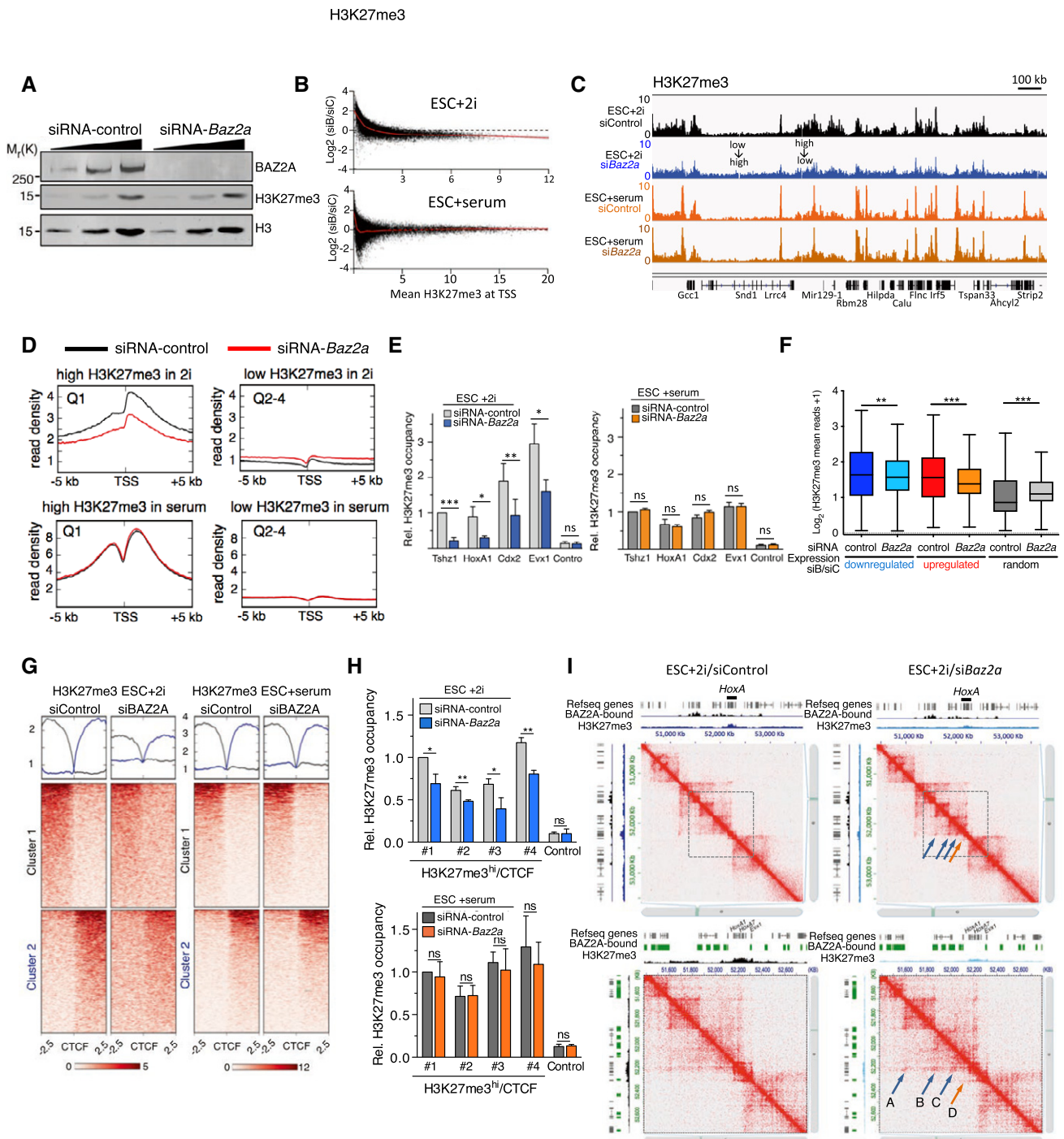

Figure 7.

◄

Figure 7. BAZ2A regulates H3K27me3 occupancy in ground-state ESCs.

A   Western blot showing total levels of H3K27me3 in ESC+2i transfected with siRNA-control and siRNA-*Baz2a*. Histone H3 is shown as a protein loading control.

B   Scatter plot showing the changes in H3K27me3 upon BAZ2A depletion in ESC+2i and ESC+serum. ESCs were subjected to two consecutive treatments with siRNA-control and siRNA-*Baz2a*, each one lasting for 4 days. Mean of normalized H3K27me3 read counts in ESC+2i and ESC+serum treated with siRNA-control or siRNA-*Baz2a* over all TSSs ($\pm$ 1 kb) were calculated. Log2-fold changes of (siRNA-*Baz2a*/siRNA-control) are plotted relative to the mean of normalized H3K27me3 occupancies. The red line represents the mean of H3K27me3 fold changes.

C   Representative images showing the H3K27me3 occupancy.

D   Average density plot of ChIP-seq read counts of H3K27me3 at $\mp$ 5 kb from the TSS of refseq genes in ESCs treated with siRNA-control or siRNA-*Baz2a* Q1: first quartile corresponding to sequences with high H3K27me3 content. Q2–4: quartiles 2–4 corresponding to sequences with low H3K27me3 content.

E   ChIP-qPCR of H3K27me3 in ESC+2i and ESC+serum treated with siRNA-control or siRNA-*Baz2a*. Data were measured by qPCR and normalized to input and to *Tshz1* value in control cells. Control represents an intergenic sequence that does not contain H3K27me3. Average values of three independent experiments. Error bars represent s.d. Statistical significance (*P*-values) for the experiments was calculated using the paired two-tailed *t*-test (ns: non-significant, * < 0.05, ** < 0.01, *** < 0.001).

F   Box plot showing changes in H3K27me3 in ESC+2i upon BAZ2A at BAZ2A-regulated and random genes. Mean of normalized H3K27me3 read counts in ESC+2i treated with siRNA-control or siRNA-*Baz2a* over TSSs ($\pm$ 1 kb) of upregulated, downregulated, and random genes were calculated. Log2-fold changes of (siRNA-*Baz2a*/siRNA-control) are plotted. Statistical significance (*P*-values) for the experiments was calculated using the paired two-tailed *t*-test (** < 0.01 and *** < 0.001). Box plots depict the minimum and maximum values. The mean is represented by a horizontal line within the boxes.

G   Average density and heat map profile of H3K27me3 transition state regions marked by CTCF sites in ESC+2i or ESC+serum transfected with siRNA-control or siRNA-*Baz2a*. Data were ranked by H3K27me3 content in the corresponding siRNA-control ESCs. Cluster 1 represents high to low H327me3 transition whereas Cluster 2 shows low to high H3K27me3 levels.

H   H3K27me3 ChIP-qPCR in ESC+2i (top panel) or ESC+serum (bottom panel) transfected with siRNA-control or siRNA-*Baz2a*. Values show H3K27me3 occupancy at four sequences (#1-#4) with elevated H3K27me3 at CTCF boundary (H3K27me3^{hi}/CTCF). Control represents an intergenic sequence that does not contain H3K27me3. Data were measured by qPCR and normalized to input and to sequence #1 value in control cells. Average values of three independent experiments. Error bars represent s.d. Statistical significance (*P*-values) for the experiments was calculated using the paired two-tailed *t*-test (ns: non-significant, * < 0.05, ** < 0.01).

I   Hi-C contact matrices for a zoomed in region on chromosome 6 containing *HoxA* cluster (10-kb resolution in upper panels, 5 kb resolution in lower panels). Blue arrows (A, B, and C) indicate gain or increase of contacts in ESC+siRNA-*Baz2a* compared with control cells (siRNA-control). The orange arrow (D) indicates loss or decrease in contacts. Quantifications are shown in Table EV5.

detectable. In contrast, BAZ2A depletion did not affect the occupancy of SMC1a at selected cohesin-bound regions in ESC+2i (Fig EV5F). The same analysis of TOP2A occupancy could not be performed due to technical issues in generating a specific TOP2A ChIP signal.

The association of BAZ2A with two important chromatin regulators such as TOP2A and cohesin provides further evidence that BAZ2A acts on chromatin of ground-state ESCs. Furthermore, the data show that TOP2A is required for BAZ2A binding to chromatin thereby phenocopying the two readouts of BAZ2A function in ESC+2i, regulation of gene expression and H3K27me3 occupancy.

Discussion

Chromatin has the intrinsic property to segregate into subnuclear compartments forming long-distance contacts between domains with similar chromatin states (Rao *et al*, 2014). In this work, we made use of the two closely and developmentally related ESC types, ground-state and developmentally advanced ESCs, to elucidate how their genome organization is regulated. We showed that both pluripotent ESC types display similar genome compartmentalization despite their different chromatin and epigenetic features. However, only ground-state ESCs rely on BAZ2A, a component of the nucleolar remodeling complex NoRC (Strohner *et al*, 2001; Santoro *et al*,

Figure 8. BAZ2A associates with TOP2A and components of the cohesin complex on chromatin.

A   Scheme representing the strategy used to identify protein interacting with BAZ2A on chromatin (Chromatin IP).

B   BAZ2A-interacting proteins on chromatin. Mass spectrometry analysis of FLAG immunoprecipitates from wt and F/H-BAZ2A ESC+2i. Values of peptide number are shown as the difference between peptides obtained in FLAG-IP of F/H-BAZ2A and wt ESC chromatin extracts. Data are from three independent experiments. The proteins found enriched in FLAG-IP of F/H-BAZ2A ESCs in all three experiments are shown. Further BAZ2A-interacting proteins identified in only two or one of the immunoprecipitation (IP) experiments are listed in Table EV6. Error bars represent s.d.

C   Anti-HA IP of wt- and F/H-BAZ2A-ESC+2i and ESC+serum. Western blot shows the interaction of BAZ2A with SNF2H, TOP2A, and SMC1a.

D   TOP2A and BAZ2A regulate gene expression in ESC+2i via a shared pathway. qRT–PCR of genes regulated by BAZ2A in ESC+2i (left panel) and in ESC+serum (right panel) upon TOP2A or BAZ2A knockdown by siRNA. ESCs were treated with the corresponding RNAs for 4 days. Upregulated genes in ESC+2i upon BAZ2A-KD are labeled in blue, downregulated genes are in red. *Nanog*, *Rex1*, and *Actin* B (*ActB*) are shown as genes not regulated by BAZ2A. mRNA levels were normalized to *Rps12* mRNA and to ESCs transfected with siRNA-Control. Average values of three independent experiments. Error bars represent s.d. Statistical significance (*P*-values) for the experiments was calculated using the paired two-tailed *t*-test (ns: non-significant, * < 0.05, ** < 0.01, *** < 0.001, **** < 0.0001).

E   Inhibition of type 2 topoisomerase activity phenocopies the alterations in gene expression of BAZ2A-regulated genes in ESC+2i observed upon TOP2A or BAZ2A knockdown. ESCs were treated with the TOP2 inhibitor ICF-193 for 24 h. mRNA levels were normalized to *Rps12* mRNA and to ESCs treated with DMSO. Upregulated genes in ESC+2i upon BAZ2A-KD are labeled in blue, downregulated genes are in red. Average values of three independent experiments. Error bars represent s.d. Statistical significance (*P*-values) for the experiments was calculated using the paired two-tailed *t*-test (ns: non-significant, ** < 0.01, *** < 0.001, **** < 0.0001).

F   ChIP analysis showing that TOP2A regulates H3K27me3 occupancy in ESC+2i but not in ESC+serum. Data were measured by qPCR and normalized to input and to *Tshz1* value in cells transfected with siRNA-control. #1-#4 indicated sequences with elevated H3K27me3 at CTCF boundary (H3K27me3^{hi}/CTCF). Control represents an intergenic region that does not contain H3K27me3. Average values of three independent experiments. Error bars represent s.d. Statistical significance (*P*-values) for the experiments was calculated using the paired two-tailed *t*-test (ns: non-significant, * < 0.05, ** < 0.01, *** < 0.001).

▶
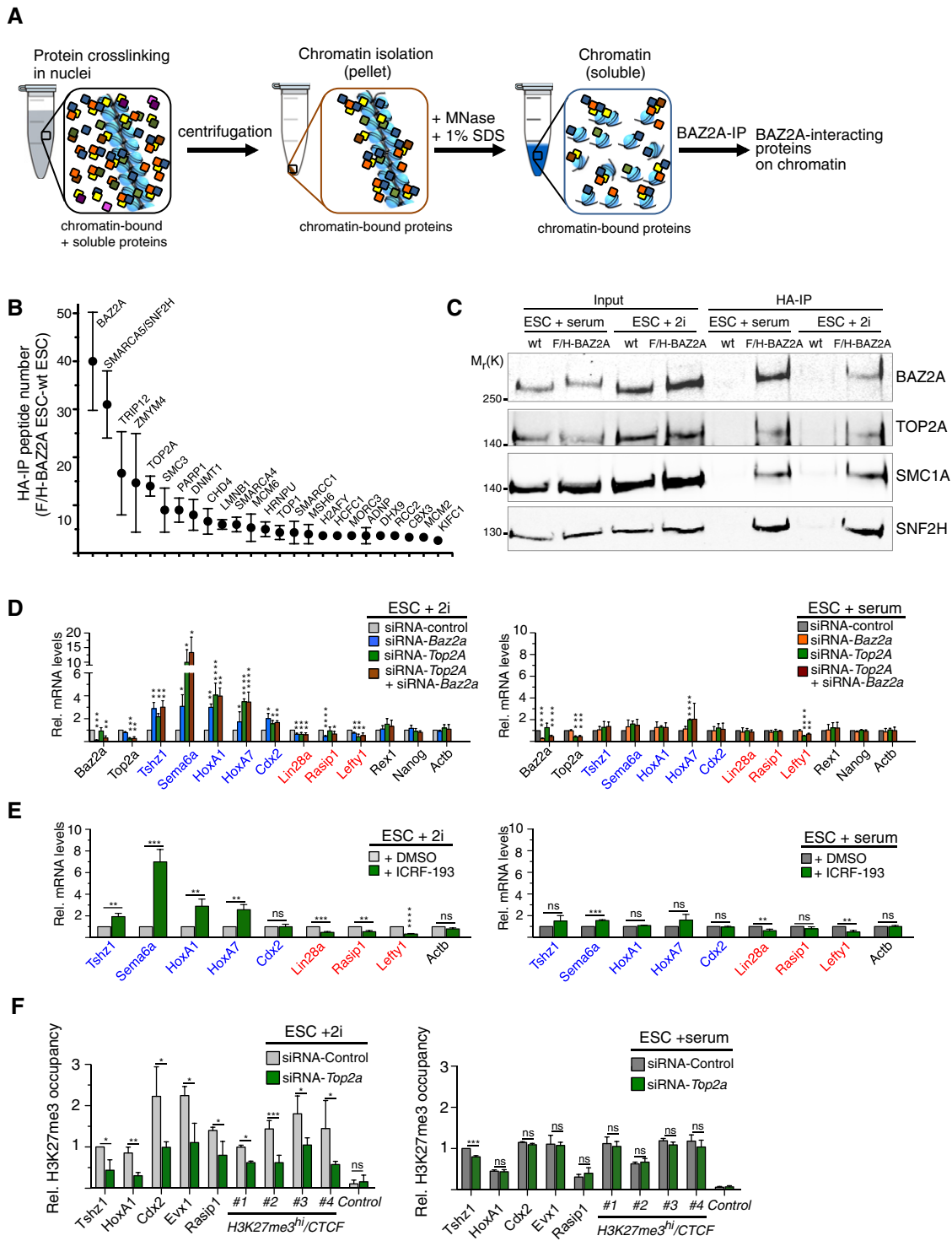
Figure 8.

2002). The role of BAZ2A appeared ground-state-specific since the absence of BAZ2A in ESC+2i, but not in ESC+serum, led to changes in self-renewal, differentiation capacity, chromatin structures, H3K27me3 occupancy, and gene expression. Importantly, alterations in chromatin accessibility, H3K27me3 occupancy, and gene expression in ESC+2i were not a consequence of BAZ2A binding to

any of these affected sites. One example of this is that BAZ2A depletion in ESC+2i leads to increased chromatin accessibility and upregulation of genes at the repressive B compartments that are not bound by BAZ2A (Appendix Fig S3A). We showed that BAZ2A binds to large and active regions of A compartments that strongly intersect through long-range contacts in ESCs. Therefore, it appears

that the function of BAZ2A in ESC+2i is on active and highly interacting chromatin domains but the effects observed upon BAZ2A depletion are mostly restricted to repressive chromatin regions. These results suggest a model where BAZ2A bound to active chromatin domains counteracts their expansion into repressed domains and this function is required only in ground-state ESCs. The possibility that active chromatin can regulate heterochromatin through indirect mechanisms has also been recently proposed by showing that MRG-1, a factor exclusively bound to euchromatin, drives spatial sequestration of heterochromatin in *C. elegans* nuclei (Cabianca *et al*, 2019). Given the striking similarity in the BAZ2A genomic occupancy in both pluripotent states, we propose that BAZ2A function is determined by the state of its substrate (i.e., chromatin) rather than by BAZ2A itself. Relative to ESC+serum, chromatin of ESC+2i contains a more active epigenetic signature and more open chromatin structures at the level of nucleosomes (Marks *et al*, 2012; Ficz *et al*, 2013; Habibi *et al*, 2013; Leitch *et al*, 2013; Ricci *et al*, 2015). These differences in chromatin states can affect the dependency on BAZ2A on several levels. For instance, the active chromatin of ESC+2i could promote a higher BAZ2A binding compared with ESC+serum, as also evident by the ChIP-seq results, making ESC+2i more dependent on BAZ2A. Furthermore, the open chromatin of ESC+2i might be in a more flexible and even less stable structure compared to ESC+serum, making ESC+2i more dependent on BAZ2A in limiting the invasion of active domains into repressive regions (Appendix Fig S3B). This increase in chromosome flexibility was also evident in Hi-C experiments, showing an increase of far-cis contacts upon BAZ2A depletion in ESC+2i. In contrast, the more repressive state of ESC+serum chromatin might confer a more rigid and stable structure that can be sufficient to limit excessive chromosome flexibility, making ESC+serum less dependent on BAZ2A.

Our data indicated that the tight control of genomic compartmentalization is central for the regulation of gene expression, epigenetic landscapes, and stem cell integrity. In this regard, we observed that upon BAZ2A depletion ESCs+2i proliferate significantly slower and had impaired differentiation potential, which is an important feature of pluripotency. Importantly, neither DNA methylation nor H3K27me3 have an influence on proliferation and transcription of genes regulated by BAZ2A in ESC+2i. Furthermore, changes in H3K27me3 were not a consequence of transcriptional changes since the decrease of H3K27me3 occurred at the promoters of both up- and downregulated genes and at intergenic domains as in the case of a subset of regions where CTCF sites mark transitions in H3K27me3 enrichment. It is important here to note that previous studies indicated that CTCF does not act as a direct barrier to H3K27me3 spreading (Dowen *et al*, 2014; Nora *et al*, 2017). The decrease of H3K27me3 content and structural changes at the Polycomb domains *HoxA* and *HoxB* loci that are not bound by BAZ2A suggests that insulation and reinforcement of H3K27me3 domains might occur through 3D genomic contacts. Accordingly, recent results showed that regulation of gene expression by Polycomb in ESCs also occur in a 3D interaction network (Schoenfelder *et al*, 2015). Furthermore, the appearance of new contacts between the *HoxA* cluster and active domains previously bound by BAZ2A in ESC+2i indicates that BAZ2A is also able to limit the invasion of active chromatin into repressed Polycomb domains (Appendix Fig S3A).

How BAZ2A acts on active chromatin domains in ground-state ESCs to limit their invasion into repressive domains remains

elusive and will be the focus of future studies. Previous biochemical studies suggested that BAZ2A associates with SNF2H, forming the nucleolar remodeling complex NoRC (Strohner *et al*, 2001). Accordingly, our chromatin IP analysis revealed that the strongest interacting partner of BAZ2A was SNF2H, suggesting that chromatin remodeling activities can play a role in this process. Furthermore, our results suggest that this mechanism most likely involves catalytically active TOP2A that interacts with BAZ2A on chromatin and is required for BAZ2A binding, thereby affecting gene expression and H3K27me3 occupancy similarly to BAZ2A. Interestingly, inhibition of TOP2 activity was shown to increase chromatin accessibility at H3K27me3 sites in ESCs, suggesting that TOP2 has a role in making facultative heterochromatin inaccessible genome-wide (Miller *et al*, 2017). Furthermore, recent computational modeling studies suggest that TOP2 activity could enable loop extrusion by resolving torsional stress, proposing an active role of TOP2 in restricting genome compartmentalization (Uuskula-Reimand *et al*, 2016; Nuebler *et al*, 2018). Therefore, the relief of chromatin torsional stress mediated by TOP2A might facilitate not only the access of BAZ2A on active chromatin but also to protect repressive domains by the invasion of euchromatin. In this context, the chromatin remodeling activity associated with NoRC might also promote access to TOP2A to exert its activity on genome compartmentalization.

Taken together, our results showed that open and active chromatin domains have the propensity to invade repressive regions. This action is particularly evident in the open and active genome of ground-state ESCs. The involvement of BAZ2A, as part of NoRC complex, and TOP2A suggest that this process can be limited by chromatin remodeling activities and chromatin torsional stress in order to preserve active and repressed genome partitioning and cell function and identity.

Materials and Methods

Cell culture

129/OlaHsd mouse embryonic stem cells were cultured in either 2i media composed of DMEM-F12 and Neurobasal medium (1:1, Life Technologies), supplemented with 1× N2/B27 (Life Technologies), 1× penicillin/streptomycin/l-glutamine (Life Technologies), 50 μM β-mercaptoethanol (Life Technologies), recombinant leukemia inhibitory factor, LIF (Polygene, 1,000 U/ml) and MEK and GSK3β inhibitors, 2i (Sigma CHIR99021 and PD0325901, 3 and 1 μM, respectively) or in serum medium containing DMEM (Life Technologies), 15% FCS, 1× MEM NEAA, 100 μM β-mercaptoethanol, 1× penicillin/streptomycin (Life Technologies). ESCs were seeded at a density of 50,000 cells/cm² in culture dishes (Corning® CellBIND® surface) coated with 0.1% gelatin without feeder layer. Propagation of cells was carried out every 2 days using enzymatic cell dissociation. When indicated, ESCs were treated with 1 μM Staurosporine 16 h. 2i conversions of ESC+serum were carried out for 8 days by plating the same number of ESC-wt and *Baz2a*-KO ESCs every 2 or 3 days.

Embryonic stem cells were differentiated by culturing for 48–72 h in complete medium: DMEM, 10% FCS, 1 mM sodium pyruvate (Sigma), 1× NEAA (Life Technologies), 1× penicillin/

streptomycin/l-glutamine, 100 μM β-mercaptoethanol on 0.1% gelatin-coated culture dishes.

Differentiation toward neural progenitor cells (NPCs) was obtained according to previously established protocol (Bibel *et al*, 2004). In brief, differentiation employed a suspension-based embryoid bodies formation (Bacteriological Petri Dishes, Bio-one with vents, Greiner®) in neural differentiation media (DMEM, 10% FCS, 1× MEM NEAA, 1× penicillin/streptomycin/l-glutamine, 100 μM β-mercaptoethanol). During the 8-day differentiation procedure, media were exchanged every 2 days. In the last 4 days of differentiation, the media were supplemented with 2 μM retinoic acid (RA) to generate neuronal precursors. DNMT-TKO ESCs were kindly provided by M. Okano (Tsumura *et al*, 2006). *Eed*-KO and *Ring1b*-KO ESC+2i were a gift from C. Ciaudo (ETH, Zurich).

Transfections

Embryonic stem cells were transfected with the indicated siRNAs (50 nM siRNA) using Lipofectamine® RNAiMAX (Life Technologies) in Opti-MEM® GlutaMAX™ (Life Technologies) reduced-serum medium. ESCs were seeded 2 h prior to siRNA transfection and collected 3 days after transfection if not stated differently. For analysis of differentiation potential of BAZ2A-depleted ESCs, transfected cells were re-seeded at equal cell numbers into complete differentiation medium 48 h after transfection. Survival of differentiated cells was assessed 72 h later. To measure cell proliferation, same number of cells were plated and counted after 3 days of siRNA treatment. In the case of RNA-seq, ATAC-seq, Hi-C, and ChIP-seq analyses, we performed two consecutive treatments with siRNA-control and siRNA-*Baz2a*, each one lasting for 4 days. Efficiencies of siRNA-mediated depletions were monitored by qRT–PCR. Only samples with reduction of *Baza* levels up to 70–80% were processed for further downstream analyses.

Alkaline phosphatase (AP) staining

Cells were fixed in 4% paraformaldehyde for 10 min, washed with AP buffer (100 mM Tris-Cl pH 9.5, 100 mM NaCl, 50 mM MgCl2), and then incubated for 5–10 min in BCIP®/NBT liquid substrate system (Sigma). The reaction was blocked with 10 mM Tris and 1 mM EDTA for 10 min.

ICRF-193 treatment

Embryonic stem cells were seeded 24 h prior to treatment. ICRF-193 was added directly to the medium to final concentration of 500 nM, as it has previously been reported for ESCs (Thakurela *et al*, 2013). Cells were harvested for respective experiments after 24 h of inhibitor treatment.

RNA extraction, reverse transcription, and quantitative PCR (qRT–PCR)

RNA was purified with TRIzol reagent (Life Technologies). One microgram total RNA was primed with random hexamers and reverse-transcribed into cDNA using MultiScribe™ Reverse Transcriptase (Life Technologies). The relative transcription levels were determined by normalization to *Rps12* or *beta-Actin* mRNA levels,

as indicated. qRT–PCR was performed with KAPA SYBR® FAST (Sigma) on a Rotor-Gene Q (Qiagen). Primer sequences are listed in Table EV7.

Chromatin fractionation

Embryonic stem cells were collected by trypsinization, washed once with PBS and counted. ES cell pellets were resuspended at a concentration of 10mio cells/ml in chromatin fractionation buffer (10 mM Hepes pH 7.6, 150 mM NaCl, 3 mM MgCl2, 0.5% Triton X-100, 1 mM DTT freshly supplemented with cOmplete™ Protease Inhibitor Cocktail (Roche)) and incubated for 30 min at room temperature rotating. Precipitated chromatin was fractionated by centrifugation. Total and chromatin fractionated samples were further processed by MNase (S7 Microccocal nuclease, Roche) digest for ensuring sufficient genomic DNA fragmentation. All samples were incubated in 1× Laemmli buffer (10% glycerol, 10 mM Tris pH 6.8, 2% SDS, 0.1 mg/ml bromphenolblue, 2% β-mercaptoethanol) at 95°C for 5 min and were further analyzed by Western Blotting.

Generation of FLAG/HA-BAZ2A and *Baz2a*-KO ESC

CRISPR/Cas9 cloning and targeting strategy was performed as previously described (Ran *et al*, 2013). To generate FLAG/HA-BAZ2A ESC+2i and ESC+serum, sgRNA guide sequence (GTCGTTTGCCTCCATTTCTGT) was chosen to target the BAZ2A locus on exon 3 three base pairs upstream of the ATG start codon and was cloned into pSpCas9(BB)-2A-GFP (PX458, Addgene). This plasmid was co-transfected with the HDR repair template plasmid containing the FLAG/HA inclusion flanked by 1 kb homology arms into wild-type ESCs at a molar ratio of 1:3. After 2 days, positively transfected cells were selected for GFP expression and were then further cultured for additional 3 days. Subsequently, ESCs were seeded for single cell clone isolation. Derived clones were genotyped by PCR using two different primer pairs. One PCR aimed to identify site-specific FLAG-HA inclusion, while the other PCR allowed distinguishing between inclusions in one or both alleles (as illustrated in Appendix Fig S4). The integrity of the FLAG-HA inclusion was verified by cloning the exon 3 sequences into CloneJET PCR cloning kit (Thermo Scientific) and by Sanger sequencing (Microsynth). FLAG/HA-BAZ2A ESC and ESC-wt behave similarly in terms of BAZ2A expression levels, lack of BAZ2A association with rRNA genes in ESC, proliferation, and expression of pluripotency markers. *Baz2a*-KO ESC+serum were obtained using the sgRNA guide sequence CACCGGTTTCAGTCCTGAGGCAGC. The *Baz2a*-knockout was confirmed through genotype and Western blot analyses.

Chromatin immunoprecipitation and mass spectrometric analyses

Approximately 10^8 ESCs were collected by scraping followed by washing with PBS. Nuclei were isolated by re-suspending the cells in two consecutive rounds in hypotonic buffer (10 mM Hepes pH 7.6, 1.5 mM MgCl2, 10 mM KCl, 2 mM Na3VO4 freshly supplemented with cOmplete™ Protease Inhibitor Cocktail (Roche)). The suspension was passed through a Dounce homogenizer with a loose pestle 10–20 times, and the purity of nuclei was checked under a microscope. The chromatin was then isolated and cross-linked by

re-suspending the nuclei in the chromatin fractionation/cross-linking buffer (10 mM Hepes pH 7.6, 3 mM $MgCl_2$, 150 mM NaCl, 0.5% Triton X-100, 0.5 mM dithiobis[succinimidylpropionate] (DSP, Thermo Scientific), 2 mM Na_3VO_4 supplemented with cOmplete™ Protease Inhibitor Cocktail (Roche)) and rotation at room temperature for 30 min. The cross-linking was stopped by the addition of 25 mM Tris–HCl pH 7.5. The chromatin was then isolated by centrifugation and washed twice in MNase digestion buffer (0.3 M Sucrose, 50 mM Tris–HCl pH 7.5, 30 mM KCl, 7.5 mM NaCl, 4 mM $MgCl_2$, 1 mM $CaCl_2$, 0.125% NP-40, 0.25% NaDeoxycholate, 2 mM Na_3VO_4 supplemented with cOmplete™ Protease Inhibitor Cocktail (Roche)). Digestion of chromatin into mononucleosomes was assured by digestion with 100U MNase (Roche) in MNase digestion buffer at 37°C for 1 h. SDS was then added to a final concentration of 1% followed by a 3×30 s sonication steps with a Bioruptor sonicator (Diagenode). Insoluble precipitates were removed by centrifugation, and soluble cross-linked chromatin extracts were diluted 10× in IP buffer (0.3 M Sucrose, 50 mM Tris–HCl pH 7.5, 30 mM KCl, 300 mM NaCl, 4 mM $MgCl_2$, 1 mM $CaCl_2$, 0.125% NP-40, 0.25% NaDeoxycholate, 2 mM Na_3VO_4 supplemented with cOmplete™ Protease Inhibitor Cocktail (Roche)) and 30 μl ANTI-FLAG M2 Affinity Gel (Sigma) was added to the extracts. Binding of FLAG/HA-BAZ2A was performed by incubation over night at 4°C while rotating. The beads were subsequently washed five times in wash buffer (20 mM Tris pH 7.5, 20% glycerol, 100 mM KCl, 300 mM NaCl, 1.5 mM MgCl2, 0.2 mM EDTA, 0.125% NP40, 0.25% NaDeoxycholate, 2 mM Na_3VO_4 supplemented with cOmplete™ Protease Inhibitor Cocktail (Roche)). Purified complexes were then eluted with 2 mM FLAG peptide (Sigma) in TBS buffer (50 mM Tris–HCl pH 8.0, 150 mM NaCl). Eluted proteins were precipitated with the addition of 0.25× volume of 100% trichloric acid (Sigma). Protein pellets were washed five times with cold Acetone (Merck) and submitted for subsequent mass spectrometric analyses by the Functional Genomics Center Zurich (FGCZ). The dry pellets were dissolved in 45 μl buffer (10 mM Tris + 2 mM $CaCl_2$, pH 8.2) and 5 μl of trypsin (100 ng/μl in 10 mM HCl) for digestion, which was carried out in a microwave instrument (Discover System, CEM) for 30 min at 5 W and 60°C. Samples were dried in a SpeedVac (Savant). For LC-MS/MS analysis, the samples were dissolved in 0.1% formic acid (Romil)) and an aliquot ranging from 5 to 25% was analyzed on a nanoAcquity UPLC (Waters Inc.) connected to a Q Exactive mass spectrometer (Thermo Scientific) equipped with a Digital PicoView source (New Objective). Peptides were trapped on a Symmetry C18 trap column (5 μm, 180 μm × 20 mm, Waters Inc.) and separated on a BEH300 C18 column (1.7 μm, 75 μm × 150 m, Waters Inc.) at a flow rate of 250 nl/min using a gradient from 1% solvent B (0.1% formic acid in acetonitrile, Romil)/99% solvent A (0.1% formic acid in water, Romil) to 40% solvent B/60% solvent A within 90 min. Mass spectrometer settings were as follows: Data-dependent analysis. Precursor scan range 350–1,500 m/z, resolution 70,000, maximum injection time 100 ms, threshold 3e6. Fragment ion scan range 200–2,000 m/z, Resolution 35,000, maximum injection time 120 ms, threshold 1e5. Proteins were identified using the Mascot search engine (Matrix Science, version 2.4.1). Mascot was set up to search the SwissProt database assuming the digestion enzyme trypsin. Mascot was searched with a fragment ion mass tolerance of 0.030 Da and a parent ion tolerance of 10.0 PPM. Oxidation of

methionine was specified in Mascot as a variable modification. Scaffold (Proteome Software Inc.) was used to validate MS/MS-based peptide and protein identifications. Peptide identifications were accepted if they achieved a false discovery rate (FDR) of less than 0.1% by the Scaffold Local FDR algorithm. Protein identifications were accepted if they achieved an FDR of less than 1.0% and contained at least two identified peptides.

Chromatin immunoprecipitation (ChIP)

ChIP analysis was performed as previously described (Leone *et al*, 2017). Briefly, 1% formaldehyde was added to cultured cells to cross-link proteins to DNA. For histone ChIPs, isolated nuclei were then lysed and sonicated using a Bioruptor ultrasonic cell disruptor (Diagenode) to shear genomic DNA to an average fragment size of 200 bp. Twenty microgram of chromatin was diluted to a total volume of 500 μl with ChIP buffer (16.7 mM Tris–HCl, pH 8.1, 167 mM NaCl, 1.2 mM EDTA, 0.01% SDS, 1.1% Triton X-100) and pre-cleared with 10 μl packed Sepharose beads for 2 h at 4°C. Pre-cleared chromatin was incubated overnight with the indicated antibodies. The next day, Dynabeads protein A (or protein G, Millipore) were added and incubated for 4 h at 4°C. After washing, bound chromatin was eluted with the elution buffer (1% SDS, 100 mM $NaHCO_3$). Upon proteinase K digestion (50°C for 3 h) and reversion of cross-linking (65°C, overnight), DNA was purified with phenol/chloroform, ethanol precipitated and quantified by qPCR using the primers listed in Table EV7.

For BAZ2A ChIPs, we noticed that sonication of formaldehyde-cross-linked chromatin-induced degradation of BAZ2A. Therefore, to increase the efficiency of BAZ2A ChIP-seq, we fragmented cross-linked chromatin into mononucleosomes through digestion with MNase. Briefly, isolated and cross-linked nuclei were MNase digested in 400 μl MNase digestion buffer (0.3 M Sucrose, 50 mM Tris pH 7.5, 30 mM KCl, 7.5 mM NaCl, 4 mM $MgCl_2$, 1 mM $CaCl_2$, 0.125% NP-40, 0.25% NaDeoxycholate, 2 mM Na_3VO_4 supplemented with cOmplete™ Protease Inhibitor Cocktail (Roche)) with 100 U MNase (Roche) at 37°C for 1 h. The digestion was then stopped with 5 mM EDTA, and the digested chromatin was solubilized in 1% SDS and three pulses of 30sec sonication using a Bioruptor ultrasonic cell disruptor (Diagenode). Chromatin size was always verified by agarose gel electrophoresis and only samples with DNA size ranging between 150 and 300 bp were used for ChIP experiments. Two hundred microgram of pre-cleared chromatin was immunopurified with incubation of 30 μl of Anti-FLAG M2 Affinity Gel (Sigma) or 30 μl Anti-HA magnetic beads (Pierce) over night. The samples were subsequently washed and eluted, and the DNA was purified as for histone ChIPs. ChIP-qPCR measurements were performed with KAPA SYBR® FAST (Sigma) on a Rotor-Gene Q (Qiagen) always comparing enrichments over input samples. Primer sequences are listed in Table EV7.

For ChIP-seq analyses, the quantity and quality of the isolated DNA were determined with a Qubit® (1.0) Fluorometer (Life Technologies, California, USA) and a Bioanalyzer 2100 (Agilent, Waldbronn, Germany). The Nugen Ovation Ultra Low Library Systems (Nugen, Inc, California, USA) was used in the following steps. Briefly, ChIP samples (1 ng) were end-repaired and polyadenylated before the ligation of Illumina compatible adapters. The adapters contain the index for multiplexing. The quality and quantity of the

enriched libraries were validated using Qubit® (1.0) Fluorometer and the Bioanalyzer 2100 (Agilent, Waldbronn, Germany). The libraries were normalized to 10 nM in Tris-Cl 10 mM, pH8.5 with 0.1% Tween 20. The TruSeq SR Cluster Kit v4-cBot-HS (Illumina, Inc, California, USA) was used for cluster generation using 8 pM of pooled normalized libraries on the cBOT. Sequencing was performed on the Illumina HiSeq 2500 single end 126 bp using the TruSeq SBS Kit v4-HS (Illumina, Inc, California, USA).

ChIP-seq data analysis

Own and published ChIP-seq reads were aligned to the mouse mm10 reference genome using Bowtie2 (version 2.2.5; Langmead & Salzberg, 2012). Read counts were computed and normalized using "bamCoverage" from deepTools (version 2.0.1; Ramirez *et al*, 2014) using a bin size of 50 bp. deepTools was also further used to generate all heat maps, profiles, and Pearson's correlation plots. BAZ2A bound regions were defined using SICER (version 1.1; Zang *et al*, 2009) by comparing the FLAG ChIPs of tagged vs non-tagged BAZ2A ESCs in 2i and serum using the following arguments: W = 1,000 G = 3,000 FDR = 0.00001. These analyses revealed 8824 and 7221 BAZ2A-bound regions in 2i and serum ESCs, respectively. Highly similar results were obtained by defining BAZ2A bound regions comparing the FLAG ChIPs to the input samples, excluding strong biases of the FLAG antibody.

Quantitative ChIP-seq experiments were performed by spike-in ESC chromatin with 50 ng of *Drosophila* chromatin in order to compare the differences in H3K27me3 levels. ChIP experiments were performed as described above. After sequencing, reads uniquely aligned were mapped to *Drosophila* genome (dm6) and an internal normalization factor was generated for each sample according to Active Motif spike-in normalization strategy. The number of reads for ESC ChIPs were normalized by down-sampling the reads based on the spike-in normalization factor using "bamCoverage" from deepTools.

CTCF ChIP-seq data sets in 2i and serum ESCs were taken from (Beagan *et al*, 2017). CTCF peaks were defined using MACS2 (version 2.1.0; Zhang *et al*, 2008) comparing the CTCF ChIP-seq to its respective input sample with a qValue cutoff of 0.0001. Using these parameters, 56,218 and 47,245 CTCF peaks were defined in 2i and serum ESCs, respectively. The ratio of mean H3K27me3 read counts 2.5 kb upstream and downstream of each CTCF peak were calculated and served as "insulation scores". H3K27me3-insulated CTCF peaks were defined with an insulation score of >2 or <0.5. Regions with an overall average of less than 0.3 normalized read counts were excluded. This filtering resulted in 7,547 CTCF peaks (13.4% of all CTCF peaks) and 8,448 peaks (17.9% of all CTCF peaks) that were H3K27me3-insulated in 2i and serum ESCs, respectively. The accuracy of these calculations was confirmed by plotting published H3K27me3 ChIP-seq data sets from wild-type 2i and serum ESCs (Marks *et al*, 2012) over these H3K27me3-insulating CTCF peaks revealing highly similar results. Pearson's correlation plots were generated using deepTools (version 2.0.1). After removal of black-list regions, chromosome 19 was partitioned into 1 kb windows and correlation plots were computed with indicated data sets. H3K36me3 (GSM590119), H3K9me3 (GSM850407; Marks *et al*, 2012), and H3K4me1 (GSM1856424; Joshi *et al*, 2015) were taken from published ChIP-seq data sets of ESCs in 2i. For data analysis

over transcribed regions, genomic coordinates from all refseq transcripts were retrieved from Ensembl biomart. After removal of blacklist regions, normalized ChIP-seq data sets were plotted either over ± 5 kb from the TSS or over the entire transcribed region by scaling the gene length to 20 kb (+5 kb from TES and −5 kb from the TSS). For distinguishing H3K27me3-high and H3K27me3-low promoters, mean read counts ± 5 kb from each TSS were computed. The first quartile was termed as H3K27me3-high, while quartiles 2–4 were defined as H3K27me3-low. BAZ2A-bound genes were defined by an overlap of a BAZ2A-bound region with the transcribed regions of the respective gene using bedtools (version 2.24.0; Quinlan & Hall, 2010). Random genes for the analysis were selected using http://www.molbiotools.com/randomgenesetgenerator.html or excel function. Conversion of mm9 and mm10 data sets was performed using CrossMap (version 0.2.4; Zhao *et al*, 2014). Integrative Genome Viewer (IGV, version 2.3.92; Robinson *et al*, 2011) was used to visualize and extract representative ChIP-seq tracks.

RNA-seq and data analysis

Total RNA from three independent siRNA-mediated BAZ2A knock-down experiments was purified with TRIzol reagent (Life Technologies) as stated above. In order to remove DNA contaminants, the samples were treated with 1U DNaseI (Thermo Scientific) for 1 h at 37°C and the RNA samples were re-purified using TRIzol. The quality of the isolated RNA was determined with a Qubit® (1.0) Fluorometer (Life Technologies, California, USA) and a Bioanalyzer 2100 (Agilent, Waldbronn, Germany). Only those samples with a 260/280 nm ratio between 1.8–2.1 and a 28S/18S ratio within 1.5–2 were further processed. The TruSeq RNA Sample Prep Kit v2 (Illumina, Inc, California, USA) was used in the succeeding steps. Briefly, total RNA samples (100–1,000 ng) were poly A enriched and then reverse-transcribed into double-stranded cDNA. The cDNA samples was fragmented, end-repaired, and polyadenylated before ligation of TruSeq adapters containing the index for multiplexing Fragments containing TruSeq adapters on both ends were selectively enriched with PCR. The quality and quantity of the enriched libraries were validated using Qubit® (1.0) Fluorometer and the Caliper GX LabChip® GX (Caliper Life Sciences, Inc., USA). The product is a smear with an average fragment size of approximately 260 bp. The libraries were normalized to 10 nM in Tris-Cl 10 mM, pH8.5 with 0.1% Tween 20. The TruSeq SR Cluster Kit HS4000 (Illumina, Inc, California, USA) was used for cluster generation using 10 pM of pooled normalized libraries on the cBOT. Sequencing was performed on the Illumina HiSeq 4000 single-end 100 bp using the TruSeq SBS Kit HS4000 (Illumina, Inc, California, USA). Reads were aligned to the reference genome (ensembl version 82) with Subread (i.e., subjunc, version 1.4.6-p4; Liao *et al*, 2013) allowing up to 16 alignments per read (options: –trim5 10 –trim3 15 -n 20 -m 5 -B 16 -H –allJunctions). Count tables were generated with Rcount (Schmid & Grossniklaus, 2015) with an allocation distance of 100 bp for calculating the weights of the reads with multiple alignments, considering the strand information, and a minimal number of five hits. Variation in gene expression was analyzed with a general linear model in R with the package edgeR (version 3.12.0; Robinson & Oshlack, 2010) according to a crossed factorial design with two explanatory factors (i) siRNA against *Baz2a* and a mock sequence,

and (ii) ESCs grown in 2i or serum. Genes differentially expressed between specific conditions were identified with linear contrasts using trended dispersion estimates and Benjamini-Hochberg multiple testing corrections. Genes with a *P*-value below 0.05 and a minimal fold change of 1.5 were considered to be differentially expressed. These thresholds have previously been used characterizing chromatin remodeler functions (de Dieuleveult *et al*, 2016). Gene ontology analysis was performed with David Bionformatics Resource 6.8 (Huang *et al*, 2009).

ATAC-seq analysis

ATAC-seq experiments were performed in biological triplicates of mES cells grown in 2i or serum conditions. Cell pellets from 50,000 cells for each condition were freshly harvested 72 h after transfection with siRNAs against BAZ2A or a control sequence. The tagmentation reaction was performed as previously described (Buenrostro *et al*, 2013) with minor adjustments of the protocol, using the Nextera DNA Library Prep Kit (Illumina) together with the barcoded primers from the Nextera Index Kit (Illumina). In brief, an additional size selection step was performed after the first five cycles of library amplification. For this, the PCR reaction was incubated with 0.6 × volume of Ampure XP beads (Beckman Coulter) for 5 min to allow binding of high molecular weight fragments. Beads containing long DNA fragments were separated on a magnet and the supernatant containing only small DNA fragments below roughly 800 bp were cleaned up using MinElute PCR purification columns (Qiagen). All libraries were amplified for 12 cycles in total, visualized and quantified with a TapeStation2200 (Agilent), and sequenced on a Illumina HiSeq4000 instrument obtaining 125 bp single-end reads.

Raw sequencing reads were filtered for low-quality after adapter removal and aligned on mm9 using Bowtie2 with "– very sensitive" mapping parameters. PCR duplicates were removed using Picard and only uniquely mapped reads were considered for further analysis. Due to very low transposition efficiency, ESC+serum/siControl replicate 2 was excluded from any further analysis. To call differentially open chromatin sites between the various conditions, the mapped reads of all conditions were merged into one alignment file. Peaks were called on the merged sample using MACS2 with – nomodel –shift -100 –extsize 200 –keep-dup all, to obtain a consensus peak set with equal contribution of each sample independent of the respective biological treatment (Lun & Smyth, 2014). The combined peak set was used to build a count matrix using the aligned reads of the individual samples. Differential peaks between sample groups were identified using edgeR (Robinson *et al*, 2010). For this, the count matrix was filtered for peaks with low coverage across all samples based on a average CPM value < -1, resulting in a final set of 128,253 peaks with *P*-values below 0.0034. The remaining counts were normalized using the total library size as well as edgeR's TMM derived normalization factors. Between two sample groups, only regions with a log fold change above > 0.5 and a FDR value < 0.1 and group_CPM > -0.2 were considered as differentially accessible for further analysis. Identified ATAC peaks were overlapped with known genomic elements using bedtools (version 2.24.0; Quinlan & Hall, 2010) with a minimum of one bp overlap from both elements. Annotation of gained and lost ATAC peaks upon BAZ2A knockdown in ESC+2i was performed using ChIP-seeker (Yu *et al*, 2015).

Hi-C and data analysis

Hi-C experiments were performed in triplicates of ESC+2i treated with siRNA-control or siRNA-*BAZ2A*. We generated roughly 200 million valid pair end reads from ESC+2i treated with siRNA-control (95 million) and siRNA-*Baz2a* (105 million).

Five million cells were pelleted and resuspended in PBS-10% FCS. PBS-10%FCS-4% formaldehyde was added to a final concentration of 2% formaldehyde (v/v). Samples were incubated at room temperature for 10 min with mixing. Ice-cold glycine solution was added to a final concentration of 0.2 M and immediately centrifuged for 5 min at 300 *g* at 4°C. Cells were washed in 1 ml of ice-cold PBS. Pellet was flash-frozen in liquid nitrogen. Pellet was taken up and washed in 1 ml ice-cold lysis buffer1, resuspended again in 1 ml of ice-cold lysis buffer and incubated for 30 min at 4°C. Sample was pelleted and washed in 0.5 ml 1.2× DpnII buffer, resuspended in 0.5 ml of DpnII buffer again and moved to a thermomixer at 37°C and 300 rpm. SDS was then carefully added to a concentration of 0.3%, slowly suspended with a pipet and incubated for an hour. Triton X-100 was added to a concentration of 2.6%, and sample was incubated for another hour. To digest the sample, 200 units of DpnII enzyme were added for a 4 h incubation in a thermomixer at 37°C and 900 rpm; another 200 units of DpnII were added for overnight incubation. From here on, we adopted the protocol described in Rao *et al* (2014) with some adjustments. Cells were incubated for 20 min at 65°C to heat inactivate DpnII and pelleted, and 300 µl of fill-in mastermix was added (218 µl of MilliQ, 30 µl of 10× NEB buffer 2, 15 µl of 10 mM dCTP, 15 µl of 10 mM dGTP, 15 µl of 10 mM dTTP, 37.5 µl of 0.4 mM biotin-14-dATP (Life Technologies, 19524-016), 10 µl of 5 U/µl DNA Polymerase I, Large (Klenow) Fragment (NEB, M0210)). Sample was mixed by pipetting and incubated for 60 min at 37°C shaking at 300 rpm and placed at 4°C afterward. Nine hundred microlitre of ligation mix was added (120 µl 10× ligase buffer, 50 units of T4 ligase (Roche) and 770 µl MilliQ) and mixed by inverting and incubated overnight at 16°C. Sample was pelleted for 5 min at 1,000 *g* and taken up in 500 µl 10 mM Tris. Protein was degraded by adding 50 µl of 20 mg/ml proteinase K (NEB, P8102), 50 µl of 10% SDS and incubated at 55°C for 30 min. Fifty-seven microlitre of 5M of sodium chloride was then added, and the sample was incubated at 68°C overnight or for at least 1.5 h. Samples were cooled to room temperature, and DNA was purified using NucleoMag P-Beads and taken up in 5 mM Tris pH7.5. Samples were sheared to a size of 300–500 bp using a Covaris S2 focused-ultrasonicator. From here on, the protocol described in (Rao *et al*, 2014) was adopted.

FastQ files were mapped to the mouse genome (mm10) using bwa-mem (Li & Durbin, 2010) and filtered and deduplicated using HiCUP v0.5.10 (Wingett *et al*, 2015). Chromosomal interaction matrices were generated using Juicer (Durand *et al*, 2016) at 500 Kb resolution and normalized by Knight and Ruiz's matrix balancing algorithm. Biological replicates were first processed independently and inspected for clustering between BAZ2A depletion and control conditions by PCA. Next, replicates per condition were pooled to create merged contact maps that were used in the downstream analyses.

Eigenvalues of samples calculated using Juicer Eigenvector were used to annotated A and B genome compartments, and TADs were calculated using Juicer Arrowhead (Lieberman-Aiden *et al*, 2009).

To visualize the impact of *Baz2a* knockdown in chromosomal architecture, we plotted the median contact frequency from each genomic region at increasing genomic distance. ENCODE Data Analysis Consortium Blacklisted Regions (Hoffman *et al*, 2013) were excluded from the analysis.

Enrichment or depletion of genomic features was tested, relative to expectation, at sub-regions within genome compartments, defined by dividing the compartments into five equal size segments where the two outer bins represent compartment boundaries and the central bin as compartment center, using the Genome Association Tester (GAT; Heger *et al*, 2013). Specifically, sub-compartment enrichment was compared to a null distribution obtained by randomly sampling 10,000 times (with replacement) segments of the same length and matching GC content as the tested feature within all annotated compartments. The genome was also divided into segments of 10 kb and assigned to eight isochore bins to control for potential confounding variables that correlate with GC content, such as gene density, in the enrichment analysis.

Genome-wide Pearson's correlation of own and published ChIP-seq data sets with high resolution Hi-C eigenvector values (Bonev *et al*, 2017) was calculated genome-wide at 5 kb resolution using deeptools (version 2.0.1; Ramirez *et al*, 2014). Published ChIP-seq data sets were taken for CTCF GSM2259907 (Beagan *et al*, 2017), H3K9me2 GSM2051614 (von Meyenn *et al*, 2016), H3K9me3 GSM850406, H3K36me3 GSM590119 (Marks *et al*, 2012), H3K27ac GSM1856425, H3K4me1 GSM1856423, Ring1b GSM1856437 (Joshi *et al*, 2015), TOP2A GSM1110842 (Dykhuizen *et al*, 2013), and Smc3 GSM560343 (Kagey *et al*, 2010).

Quantification and statistical analysis

The number of independent experimental replications is reported in the figure legends. Statistical significance (*P*-values) was calculated using the paired or unpaired two-tailed *t*-test as specified in the corresponding figure legends. For all statistical analyses, a value of $P < 0.05$ was statistically significant.

Public data sets used in this study

Public data sets used in this study are listed in Table EV7.

Data availability

All raw data generated in this study using high-throughput sequencing are accessible through NCBI's GEO (accession number GSE112222).

Expanded View for this article is available online.

References

Akimitsu N, Adachi N, Hirai H, Hossain MS, Hamamoto H, Kobayashi M, Aratani Y, Koyama H, Sekimizu K (2003) Enforced cytokinesis without complete nuclear division in embryonic cells depleting the activity of DNA topoisomerase IIalpha. *Genes Cells* 8: 393–402

Beagan JA, Duong MT, Titus KR, Zhou L, Cao Z, Ma J, Lachanski CV, Gillis DR, Phillips-Cremins JE (2017) YY1 and CTCF orchestrate a 3D chromatin looping switch during early neural lineage commitment. *Genome Res* 27: 1139–1152

Bibel M, Richter J, Schrenk K, Tucker KL, Staiger V, Korte M, Goetz M, Barde YA (2004) Differentiation of mouse embryonic stem cells into a defined neuronal lineage. *Nat Neurosci* 7: 1003–1009

Bonev B, Mendelson Cohen N, Szabo Q, Fritsch L, Papadopoulos GL, Lubling Y, Xu X, Lv X, Hugnot JP, Tanay A *et al* (2017) Multiscale 3D genome rewiring during mouse neural development. *Cell* 171(557–572): e24

Boroviak T, Loos R, Bertone P, Smith A, Nichols J (2014) The ability of inner-cell-mass cells to self-renew as embryonic stem cells is acquired following epiblast specification. *Nat Cell Biol* 16: 516–528

Buenrostro JD, Giresi PG, Zaba LC, Chang HY, Greenleaf WJ (2013) Transposition of native chromatin for fast and sensitive epigenomic profiling of open chromatin, DNA-binding proteins and nucleosome position. *Nat Methods* 10: 1213–1218

Cabianca DS, Munoz-Jimenez C, Kalck V, Gaidatzis D, Padeken J, Seeber A, Askjaer P, Gasser SM (2019) Active chromatin marks drive spatial sequestration of heterochromatin in *C. elegans* nuclei. *Nature* 569: 734–739

de Dieuleveult M, Yen K, Hmitou I, Depaux A, Boussouar F, Dargham DB, Jounier S, Humbertclaude H, Ribierre F, Baulard C *et al* (2016) Genome-wide nucleosome specificity and function of chromatin remodellers in ES cells. *Nature*

Dixon JR, Jung I, Selvaraj S, Shen Y, Antosiewicz-Bourget JE, Lee AY, Ye Z, Kim A, Rajagopal N, Xie W *et al* (2015) Chromatin architecture reorganization during stem cell differentiation. *Nature* 518: 331–336

Dowen JM, Fan ZP, Hnisz D, Ren G, Abraham BJ, Zhang LN, Weintraub AS, Schujiers J, Lee TI, Zhao K *et al* (2014) Control of cell identity genes occurs in insulated neighborhoods in mammalian chromosomes. *Cell* 159: 374–387

Durand NC, Shamim MS, Machol I, Rao SS, Huntley MH, Lander ES, Aiden EL (2016) Juicer provides a one-click system for analyzing loop-resolution Hi-C experiments. *Cell Syst* 3: 95–98

Dykhuizen EC, Hargreaves DC, Miller EL, Cui K, Korshunov A, Kool M, Pfister S, Cho YJ, Zhao K, Crabtree GR (2013) BAF complexes facilitate decatenation of DNA by topoisomerase IIalpha. *Nature* 497: 624–627

Ficz G, Hore TA, Santos F, Lee HJ, Dean W, Arand J, Krueger F, Oxley D, Paul YL, Walter J *et al* (2013) FGF signaling inhibition in ESCs drives rapid genome-wide demethylation to the epigenetic ground state of pluripotency. *Cell Stem Cell* 13: 351–359

Guetg C, Lienemann P, Sirri V, Grummt I, Hernandez-Verdun D, Hottiger MO, Fussenegger M, Santoro R (2010) The NoRC complex mediates the heterochromatin formation and stability of silent rRNA genes and centromeric repeats. *EMBO J* 29: 2135–2146

Guetg C, Scheifele F, Rosenthal F, Hottiger MO, Santoro R (2012) Inheritance of silent rDNA chromatin is mediated by PARP1 via noncoding RNA. *Mol Cell* 45: 790–800

Haarhuis JHI, van der Weide RH, Blomen VA, Yanez-Cuna JO, Amendola M, van Ruiten MS, Krijger PHL, Teunissen H, Medema RH, van Steensel B *et al* (2017) The cohesin release factor WAPL restricts chromatin loop extension. *Cell* 169: 693–707 e14

Habibi E, Brinkman AB, Arand J, Kroeze LI, Kerstens HH, Matarese F, Lepikhov K, Gut M, Brun-Heath I, Hubner NC *et al* (2013) Whole-genome bisulfite sequencing of two distinct interconvertible DNA methylomes of mouse embryonic stem cells. *Cell Stem Cell* 13: 360–369

Hackett JA, Surani MA (2014) Regulatory principles of pluripotency: from the ground state up. *Cell Stem Cell* 15: 416–430

Heger A, Webber C, Goodson M, Ponting CP, Lunter G (2013) GAT: a simulation framework for testing the association of genomic intervals. *Bioinformatics* 29: 2046–2048

Hoffman MM, Ernst J, Wilder SP, Kundaje A, Harris RS, Libbrecht M, Giardine B, Ellenbogen PM, Bilmes JA, Birney E *et al* (2013) Integrative annotation of chromatin elements from ENCODE data. *Nucleic Acids Res* 41: 827–841

Huang W, Sherman BT, Lempicki RA (2009) Systematic and integrative analysis of large gene lists using DAVID bioinformatics resources. *Nat Protoc* 4: 44–57

Joshi O, Wang SY, Kuznetsova T, Atlasi Y, Peng T, Fabre PJ, Habibi E, Shaik J, Saeed S, Handoko L *et al* (2015) Dynamic reorganization of extremely long-range promoter-promoter interactions between two states of pluripotency. *Cell Stem Cell* 17: 748–757

Kagey MH, Newman JJ, Bilodeau S, Zhan Y, Orlando DA, van Berkum NL, Ebmeier CC, Goossens J, Rahl PB, Levine SS *et al* (2010) Mediator and cohesin connect gene expression and chromatin architecture. *Nature* 467: 430–435

Langmead B, Salzberg SL (2012) Fast gapped-read alignment with Bowtie 2. *Nat Methods* 9: 357–359

Leitch HG, McEwen KR, Turp A, Encheva V, Carroll T, Grabole N, Mansfield W, Nashun B, Knezovich JG, Smith A *et al* (2013) Naive pluripotency is associated with global DNA hypomethylation. *Nat Struct Mol Biol* 20: 311–316

Leone S, Bar D, Slabber CF, Dalcher D, Santoro R (2017) The RNA helicase DHX9 establishes nucleolar heterochromatin, and this activity is required for embryonic stem cell differentiation. *EMBO Rep* 18: 1248–1262

Li H, Durbin R (2010) Fast and accurate long-read alignment with Burrows-Wheeler transform. *Bioinformatics* 26: 589–595

Liao Y, Smyth GK, Shi W (2013) The Subread aligner: fast, accurate and scalable read mapping by seed-and-vote. *Nucleic Acids Res* 41: e108

Lieberman-Aiden E, van Berkum NL, Williams L, Imakaev M, Ragoczy T, Telling A, Amit I, Lajoie BR, Sabo PJ, Dorschner MO *et al* (2009) Comprehensive mapping of long-range interactions reveals folding principles of the human genome. *Science* 326: 289–293

Lun AT, Smyth GK (2014) *De novo* detection of differentially bound regions for ChIP-seq data using peaks and windows: controlling error rates correctly. *Nucleic Acids Res* 42: e95

Marks H, Kalkan T, Menafra R, Denissov S, Jones K, Hofemeister H, Nichols J, Kranz A, Stewart AF, Smith A *et al* (2012) The transcriptional and epigenomic foundations of ground state pluripotency. *Cell* 149: 590–604

Mayer C, Schmitz KM, Li J, Grummt I, Santoro R (2006) Intergenic transcripts regulate the epigenetic state of rRNA genes. *Mol Cell* 22: 351–361

McLaughlin K, Flyamer IM, Thomson JP, Mjoseng HK, Shukla R, Williamson I, Grimes GR, Illingworth RS, Adams IR, Pennings S *et al* (2019) DNA methylation directs polycomb-dependent 3D genome re-organization in naive pluripotency. *Cell Rep* 29: 1974–1985 e6

von Meyenn F, Iurlaro M, Habibi E, Liu NQ, Salehzadeh-Yazdi A, Santos F, Petrini E, Milagre I, Yu M, Xie Z *et al* (2016) Impairment of DNA methylation maintenance is the main cause of global demethylation in naive embryonic stem cells. *Mol Cell* 62: 983

Miller EL, Hargreaves DC, Kadoch C, Chang CY, Calarco JP, Hodges C, Buenrostro JD, Cui K, Greenleaf WJ, Zhao K *et al* (2017) TOP2 synergizes with BAF chromatin remodeling for both resolution and formation of facultative heterochromatin. *Nat Struct Mol Biol* 24: 344–352

Nitiss JL (2009) DNA topoisomerase II and its growing repertoire of biological functions. *Nat Rev Cancer* 9: 327–337

Nora EP, Goloborodko A, Valton AL, Gibcus JH, Uebersohn A, Abdennur N, Dekker J, Mirny LA, Bruneau BG (2017) Targeted degradation of CTCF decouples local insulation of chromosome domains from genomic compartmentalization. *Cell* 169: 930–944 e22

Nuebler J, Fudenberg G, Imakaev M, Abdennur N, Mirny LA (2018) Chromatin organization by an interplay of loop extrusion and compartmental segregation. *Proc Natl Acad Sci USA* 115: E6697–E6706

Peric-Hupkes D, Meuleman W, Pagie L, Bruggeman SW, Solovei I, Brugman W, Graf S, Flicek P, Kerkhoven RM, van Lohuizen M *et al* (2010) Molecular maps of the reorganization of genome-nuclear lamina interactions during differentiation. *Mol Cell* 38: 603–613

Pommier Y, Leo E, Zhang H, Marchand C (2010) DNA topoisomerases and their poisoning by anticancer and antibacterial drugs. *Chem Biol* 17: 421–433

Quinlan AR, Hall IM (2010) BEDTools: a flexible suite of utilities for comparing genomic features. *Bioinformatics* 26: 841–842

Ramirez F, Dundar F, Diehl S, Gruning BA, Manke T (2014) deepTools: a flexible platform for exploring deep-sequencing data. *Nucleic Acids Res* 42: W187–W191

Ran FA, Hsu PD, Wright J, Agarwala V, Scott DA, Zhang F (2013) Genome engineering using the CRISPR-Cas9 system. *Nat Protoc* 8: 2281–2308

Rao SS, Huntley MH, Durand NC, Stamenova EK, Bochkov ID, Robinson JT, Sanborn AL, Machol I, Omer AD, Lander ES *et al* (2014) A 3D map of the human genome at kilobase resolution reveals principles of chromatin looping. *Cell* 159: 1665–1680

Rao SSP, Huang SC, Glenn St Hilaire B, Engreitz JM, Perez EM, Kieffer-Kwon KR, Sanborn AL, Johnstone SE, Bascom GD, Bochkov ID *et al* (2017) Cohesin loss eliminates all loop domains. *Cell* 171: 305–320 e24

Ricci MA, Manzo C, Garcia-Parajo MF, Lakadamyali M, Cosma MP (2015) Chromatin fibers are formed by heterogeneous groups of nucleosomes *in vivo*. *Cell* 160: 1145–1158

Robinson MD, McCarthy DJ, Smyth GK (2010) edgeR: a Bioconductor package for differential expression analysis of digital gene expression data. *Bioinformatics* 26: 139–140

Robinson MD, Oshlack A (2010) A scaling normalization method for differential expression analysis of RNA-seq data. *Genome Biol* 11: R25

Robinson JT, Thorvaldsdóttir H, Winckler W, Guttman M, Lander ES, Getz G, Mesirov JP (2011) Integrative genomics viewer. *Nat Biotechnol* 29: 24 – 26

Santoro R, Li J, Grummt I (2002) The nucleolar remodeling complex NoRC mediates heterochromatin formation and silencing of ribosomal gene transcription. *Nat Genet* 32: 393 – 396

Savic N, Bar D, Leone S, Frommel SC, Weber FA, Vollenweider E, Ferrari E, Ziegler U, Kaech A, Shakhova O *et al* (2014) lncRNA maturation to initiate heterochromatin formation in the nucleolus is required for exit from pluripotency in ESCs. *Cell Stem Cell* 15: 720 – 734

Schmid MW, Grossniklaus U (2015) Rcount: simple and flexible RNA-Seq read counting. *Bioinformatics* 31: 436 – 437

Schoenfelder S, Sugar R, Dimond A, Javierre BM, Armstrong H, Mifsud B, Dimitrova E, Matheson L, Tavares-Cadete F, Furlan-Magaril M *et al* (2015) Polycomb repressive complex PRC1 spatially constrains the mouse embryonic stem cell genome. *Nat Genet* 47: 1179 – 1186

Schwarzer W, Abdennur N, Goloborodko A, Pekowska A, Fudenberg G, Loe-Mie Y, Fonseca NA, Huber W, Haering CH, Mirny L *et al* (2017) Two independent modes of chromatin organization revealed by cohesin removal. *Nature* 551: 51 – 56

Strohner R, Nemeth A, Jansa P, Hofmann-Rohrer U, Santoro R, Langst G, Grummt I (2001) NoRC–a novel member of mammalian ISWI-containing chromatin remodeling machines. *EMBO J* 20: 4892 – 4900

Thakurela S, Garding A, Jung J, Schubeler D, Burger L, Tiwari VK (2013) Gene regulation and priming by topoisomerase IIalpha in embryonic stem cells. *Nat Commun* 4: 2478

Tiwari VK, Burger L, Nikoletopoulou V, Deogracias R, Thakurela S, Wirbelauer C, Kaut J, Terranova R, Hoerner L, Mielke C *et al* (2012) Target genes of Topoisomerase IIbeta regulate neuronal survival and are defined by their chromatin state. *Proc Natl Acad Sci USA* 109: E934 – E943

Tsumura A, Hayakawa T, Kumaki Y, Takebayashi S, Sakaue M, Matsuoka C, Shimotohno K, Ishikawa F, Li E, Ueda HR *et al* (2006) Maintenance of self-renewal ability of mouse embryonic stem cells in the absence of DNA methyltransferases Dnmt1, Dnmt3a and Dnmt3b. *Genes Cells* 11: 805 – 814

Uuskula-Reimand L, Hou H, Samavarchi-Tehrani P, Rudan MV, Liang M, Medina-Rivera A, Mohammed H, Schmidt D, Schwalie P, Young EJ *et al* (2016) Topoisomerase II beta interacts with cohesin and CTCF at topological domain borders. *Genome Biol* 17: 182

Wingett S, Ewels P, Furlan-Magaril M, Nagano T, Schoenfelder S, Fraser P, Andrews S (2015) HiCUP: pipeline for mapping and processing Hi-C data. *F1000Res* 4: 1310

Ying QL, Wray J, Nichols J, Batlle-Morera L, Doble B, Woodgett J, Cohen P, Smith A (2008) The ground state of embryonic stem cell self-renewal. *Nature* 453: 519 – 523

Yu G, Wang LG, He QY (2015) ChIPseeker: an R/Bioconductor package for ChIP peak annotation, comparison and visualization. *Bioinformatics* 31: 2382 – 2383

Zang C, Schones DE, Zeng C, Cui K, Zhao K, Peng W (2009) A clustering approach for identification of enriched domains from histone modification ChIP-Seq data. *Bioinformatics* 25: 1952 – 1958

Zhang Y, Liu T, Meyer CA, Eeckhoute J, Johnson DS, Bernstein BE, Nusbaum C, Myers RM, Brown M, Li W *et al* (2008) Model-based analysis of ChIP-Seq (MACS). *Genome Biol* 9: R137

Zhao H, Sun Z, Wang J, Huang H, Kocher JP, Wang L (2014) CrossMap: a versatile tool for coordinate conversion between genome assemblies. *Bioinformatics* 30: 1006 – 1007